PRELAUNCH STUDY

REPORT OF VAS-D PERFORMANCE

A REPORT

from the space science and engineering center
the university of wisconsin-madison
madison, wisconsin

PRELAUNCH STUDY
REPORT OF VAS-D PERFORMANCE

A Report Under NASA Contract NAS5-21965

by

Paul Menzel

September 1980

The University of Wisconsin
Space Science and Engineering Center
1225 West Dayton Street
Madison, Wisconsin 53706

TABLE OF CONTENTS

INTRODUCTION

With the launch of GOES-D in September 1980, the first VISSR Atmospheric Sounder (VAS) instrument will be placed in geostationary orbit. The VAS program has the goal of timely observation and analysis of short-lived weather phenomena. Whether or not that goal can be achieved will depend largely on the VAS instrument performance in three areas -- radiometric calibration, noise reduction and registration of different spectral bands. These are the areas where the VAS instrument differs most significantly from the existing VISSRs.

To calibrate the VAS an accurate evaluation of the telescope contributions to the radiative background must be made. A radiative model was developed and tested so that calibration can be accomplished by monitoring the temperatures of key telescope components and calculating their individual radiative properties as a function of wavelength and temperature.

The VAS can determine spectral radiances over regions of interest to the required sounding accuracy of .25 ergs/(sec · ster · cm^2 · cm^{-1}) only by averaging many individual measurements. Each of these individual measurements has noise contributions that are significantly correlated to noise on the preceding and following measurements. The effects of noise correlation were investigated and a prelaunch spin budget was determined.

To determine accurate soundings the different spectral bands of the VAS must view the same scene within the same field of view. A number of registration errors have been identified that make identical spatial weighting impossible. These errors were enumerated and their combined effect on clear column radiance retrieval for sounding applications were numerically simulated.

The prelaunch study at the University of Wisconsin was focused on analyzing vacuum test data to verify instrument performance in these areas. This document presents the results of these analyses.

I. VAS RADIOMETRIC CALIBRATION

The VISSR Atmospheric Sounder (VAS) will expose photoconductive HgCdTe and InSb detectors to filtered and focused radiation emitted from the earth. The resulting detector output voltage must be converted to spectral radiance values by a reliable calibration procedure. The VAS detectors have a linear relationship between output voltage and input radiance which is determined by voltage responses to two known radiances.

Explanation of the Calibration Algorithm

To see this more clearly consider the voltage response of a linear radiometer

$$V_T = \alpha N_T + V_0 \tag{I.1}$$

where V_T is the target output voltage, N_T is the target input radiance, α is the responsivity of the radiometer, and V_0 is the system offset voltage. Calibration consists of determining α and V_0. A rigorous determination is made by exposing the radiometer to the two different external radiation targets of known radiance magnitude and measuring radiometer responses. Therefore, if Z refers to a space view and B refers to an external blackbody view, we have

$$V_Z = \alpha N_Z + V_0,$$

$$V_B = \alpha N_B + V_0,$$

so

$$\alpha = (V_B - V_Z)/(N_B - N_Z), \tag{I.2}$$

$$V_0 = (N_B V_Z - N_Z V_B)/(N_B - N_Z). \tag{I.3}$$

But the space view through the telescope delivers approximately zero radiance so $N_Z = 0$, so target radiance as a function of detector voltage response is

$$N_T = (N_B V_T - N_B V_Z)/(V_B - V_Z). \tag{I.4}$$

However, this relationship assumes that there is a source of known radiance external to VAS. This is not so. Instead an internal blackbody is used for calibration from which an effective value for N_B must be determined. The radiometric model to estimate the effective value of N_B is based on optical constants of the VAS telescope and temperature measurements of the optical components. The accuracy of the calibration is limited to the accuracy of the constants and temperatures used to estimate N_B.

A simplified description of the VAS and its radiation sources and targets is presented in Figure I.1. The VAS detector responds to the combined radiation from the target and the telescope, except when a shutter is inserted and then it responds to radiation from an internal blackbody. Thus, there are three distinct measurements which must be considered in the VAS calibration. They are,

space view: $$V_Z = \alpha(\gamma N_Z^{0} + (1 - \gamma)N_V) + V_0 \qquad (I.5)$$

internal blackbody: $$V_I = \alpha N_I + V_0 \qquad (I.6)$$

external target: $$V_T = \alpha(\gamma N_T + (1 - \gamma)N_V) + V_0 \qquad (I.7)$$

where γ is the transmittance of the VAS telescope, N_V is the radiance emanating from the VAS telescope, N_I is the radiance detected during the internal blackbody view and V_I is the associated output voltage. Equations (I.5) and (I.7) imply

$$N_T = (V_T - V_Z)/\alpha\gamma, \qquad (I.8)$$

and (I.5) and (I.6) yield

$$\alpha = (V_I - V_Z)(N_I - (1 - \gamma)N_V)^{-1}. \qquad (I.9)$$

So (I.9) into (I.8) says

$$N_T = \frac{V_T - V_Z}{V_I - V_Z} \frac{(N_I - (1 - \gamma)N_V)}{\gamma}. \qquad (I.10)$$

Comparing (I.10) and (I.4), we realize that an expression for the effective value of N_B has been determined

$$N_B = \frac{N_I - (1 - \gamma)N_V}{\gamma}. \qquad (I.11)$$

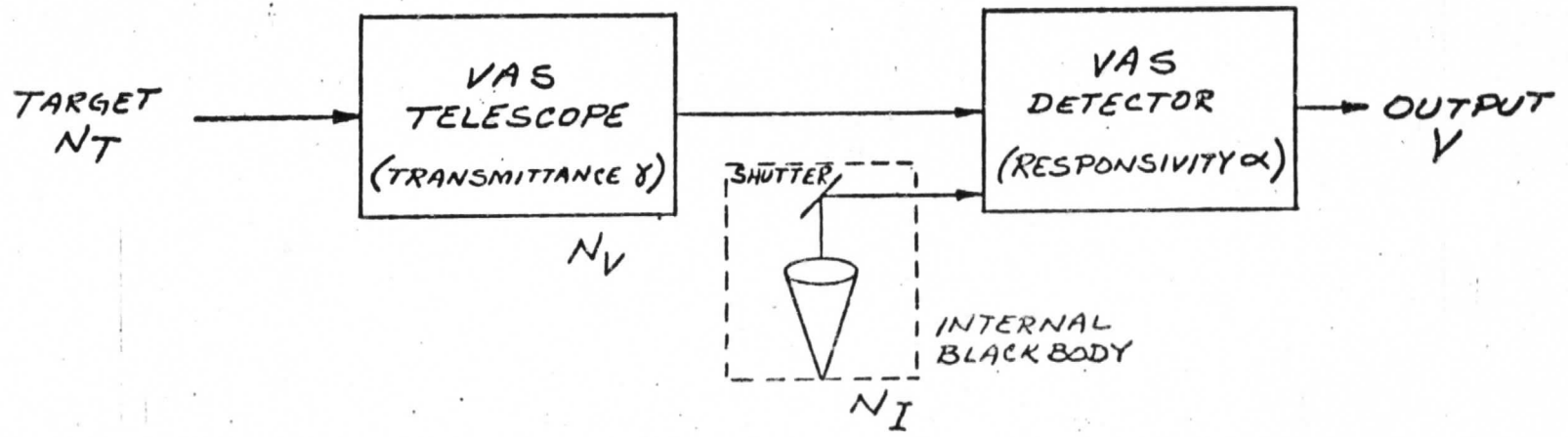

SHUTTER IS INSERTED INTO DETECTOR FIELD OF VIEW FOR PART OF EVERY SPIN OF INSTRUMENT.

SIMPLIFIED DESCRIPTION OF VAS INSTRUMENT

FIGURE I.1

An external blackbody of radiance N_B causes the same detector response as an internal blackbody of radiance N_I.

A rigorous determination of N_I must include radiative contributions from both the internal blackbody, R_{bb}, and the shutter cavity in which the reflecting mirror rests, R_{sc}. Therefore, if ε is the emissivity of the shutter cavity

$$N_I = (1-\varepsilon)R_{bb} + \varepsilon R_{sc}. \tag{I.12}$$

The radiance of the VAS telescope has been modelled so that

$$(1 - \gamma)N_V = \sum_i a_i R(T_i) \tag{I.13}$$

with the constraint

$$\sum_i a_i = (1 - \gamma), \tag{I.14}$$

where $\sum_i$ runs over all telescope foreoptics components that contribute appreciably to the background radiation, the a_i are constants determined from the reflectivities, emissivities, and obscuration fractions of the various telescope components, T_i is the temperature of a given foreoptics component, and $R(T_i)$ represents the radiance from that component. For a given spectral band of spectral response $F(\nu)$, where ν is frequency, then

$$R(T) = \int_0^\infty B(T,\nu)F(\nu)d\nu \;/\; \int_0^\infty F(\nu)d\nu \tag{I.15}$$

where $B(T,\nu)$ is the Planck function.

Thus, we can rewrite (I.11) so that it reads

$$N_B = \frac{1}{\gamma} N_I - \frac{1}{\gamma} \sum_i a_i R(T_i) \tag{I.16}$$

and with (I.12)

$$N_B = \frac{1}{\gamma} R_{bb} - \frac{1}{\gamma} \varepsilon R_{bb} + \varepsilon R_{sc} - \frac{1}{\gamma} \sum_i a_i R(T_i). \tag{I.17}$$

Using (I.13),

$$N_B = R_{bb} + \frac{1}{\gamma} \sum_i a_i (R_{bb} - R(T_i)) - \frac{\varepsilon}{\gamma} (R_{bb} - R_{sc}). \tag{I.18}$$

Define Σ'_i to be the sum over the foreoptics components plus the shutter cavity, and let $a_{sc} = -\varepsilon$.

$$N_B = R_{bb} + \frac{1}{\gamma} \Sigma'_i a_i \, (R_{bb} - R(T_i)). \qquad \text{(I.19)}$$

Define $c_i = a_i/\gamma$, then the calibration equation reads

$$N_T = \frac{V_T - V_Z}{V_I - V_Z} \{ R_{bb} + \Sigma_i c_i (R_{bb} - R(T_i)) \}. \qquad \text{(I.20)}$$

Figure I.2 shows an optical schematic of the VAS telescope and the eight components that are part of the sum Σ'. Table I.1 lists the ray trace determination of these eight coefficients and gives an error estimate due to uncertainties in the obscuration fractions (nominally .01) and the reflectances (nominally .01).

Vacuum Test Results

The VAS Engineering Model Thermal Vacuum Test of spring 1976 attempted to verify that this calibration technique met the accuracy requirements 1.5°C absolute error (mean error) and .5°C relative error (standard deviation). The evaluation of the calibration accuracy was somewhat obscured by preamplifier dc restore problems. However, it was possible to obtain a good data set of temperatures and voltages for spectral band 8. Band 8 calibration accuracy was evaluated for 20 different telescope temperature conditions from essentially isothermal to a gradient of approximately 18°C. The relative error was found to be 1.2°C, well outside of the accuracy requirements. Investigation of the data revealed that the baffle forward (BF) and the secondary mirror shield (SMS) components of the telescope foreoptics contributed roughly two-thirds of the total telescope correction. Efforts to determine these two coefficients by regression analysis from the data was unsuccessful because the temperature gradients of these two components were highly correlated.

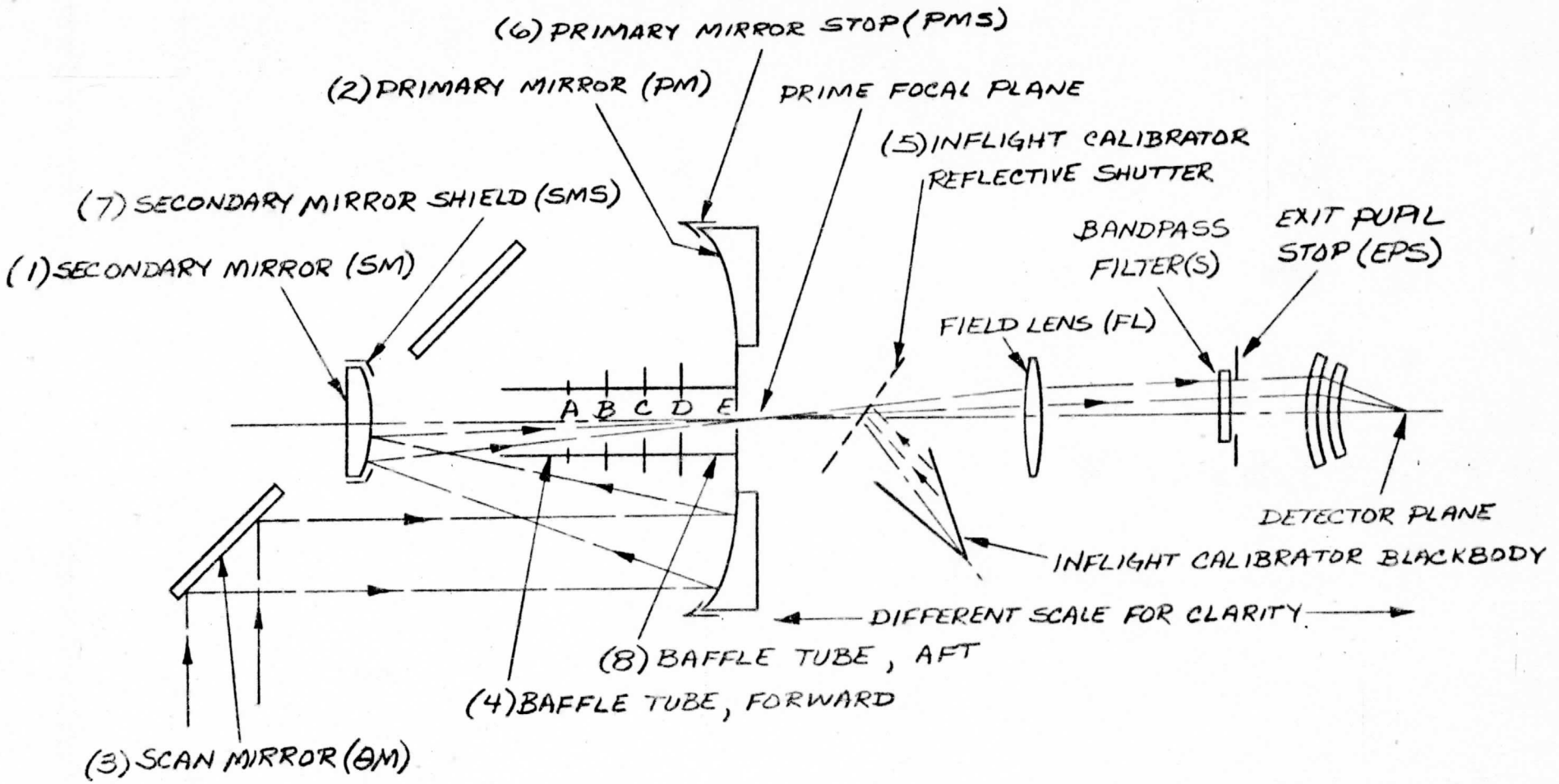

OPTICAL SCHEMATIC FOR INFLIGHT RADIOMETRIC CALIBRATION ANALYSIS

FIGURE I.2

Table I.1. VAS-D Radiometric Calibration Algorithm Coefficients

i	Symbol	Component Name	Functional Expression	Ray Trace Value
1	SM	Secondary Mirrory	$(1-K_{EB}-K_{SMS})(1-\rho_{SM})/(K_{NF}\rho_{\theta M}\rho_{PM}\rho_{SM})$	.041 ± .014
2	PM	Primary Mirror	$(1-\rho_{PM})/(\rho_{\theta M}\rho_{PM})$	.032 ± .011
3	θM	Scan Mirror	$(1-\rho_{\theta M})/\rho_{\theta M}$	.031 ± .010
4	NG	Baffle Forward	$0.65(K_{CO}\rho_{SM}+K_{EB})/(K_{NF}\rho_{\theta M}\rho_{PM}\rho_{SM})$	.168 ± .015
5	SC	Shutter Cavity	$-\varepsilon/K_{NF}\rho_{\theta M}\rho_{PM}\rho_{SM}$	-.031 ± .016
6	PMM	Primary Mirror Mask	$K_{PMM}/(K_{NF}\rho_{\theta M}\rho_{PM})$	.042 ± .016
7	SMS	Secondary Mirror Shield	$K_{SMS}/(K_{NF}\rho_{\theta M}\rho_{PM}\rho_{SM})$	.228 ± .017
8	BA	Baffle Aft	$0.35(K_{CO}\rho_{SM}+K_{EB})/(K_{NF}\rho_{\theta M}\rho_{PM}\rho_{SM})$	.0903 ± .008

Where K_{NF} (normalizing factor) $= 1-K_{CO}-K_{EB}-K_{SMS}-K_{PMM}$

$K_{CO} = .128$ = Central obscuration to exit pupil stop ratio

$K_{EB} = .0342$ = Extra beam contribution to exit pupil stop ratio

$K_{SMS} = .1400$ = Secondary mirror shield to exit pupil stop ratio

$K_{PMM} = .0261$ = Primary mirror mask to exit pupil stop ratio

$\rho_{\theta M} = \rho_{PM} = \rho_{SM} = .97$ = Reflectance value of associated mirror surface

$\gamma = .61304$

$= K_{NF}\rho_{\theta M}\rho_{SM}\rho_{PM}$ = Transmittance of VAS telescope

$\varepsilon = .02$ = Emissivity of shutter

At this time it was decided that the most significant improvement in the calibration would be realized from accurate determination of the baffle forward and secondary mirror shield coefficients. Variation of the temperature gradients with respect to the internal blackbody of especially these two components during the Calibration and Acceptance Test should be uncorrelated and should allow unique determination of these coefficients. In addition, telescope temperature gradients should be as close as possible to those expected in space so that possible non-unique coefficient changes from the ray trace value based on test data would be representative.

These goals were accomplished in the Calibration and Acceptance Test of fall 1979. Calibration accuracy was evaluated for 28 different telescope temperature conditions from essentially isothermal to a gradient of roughly 21°C with respect to the internal blackbody. Figure I.3 summarizes the main features of these gradients. Figure I.4 shows the test configuration.

A brief explanation of the data gathered and the analysis attempted follows. Three detector voltages were measured: the external target signal, V_E; the internal blackbody signal, V_I; and the space or offset signal, V_Z. Twelve temperatures were measured: T_{bb}, T_i, T_9 = temperature of the five-position mirror in the calibrator, T_{10} = temperature of the calibrator mirror, and T_{ET} = temperature of the external target. Two additional terms were required in the algorithm evaluation of the effective blackbody radiance N_B when the calibrator was used. To determine the effective blackbody radiance of the VAS internal blackbody when placed external to the VAS and the calibrator, the effect of the calibrator 5-position mirror (5PM) and the calibrator telescope optics (CM) had to be taken into account.

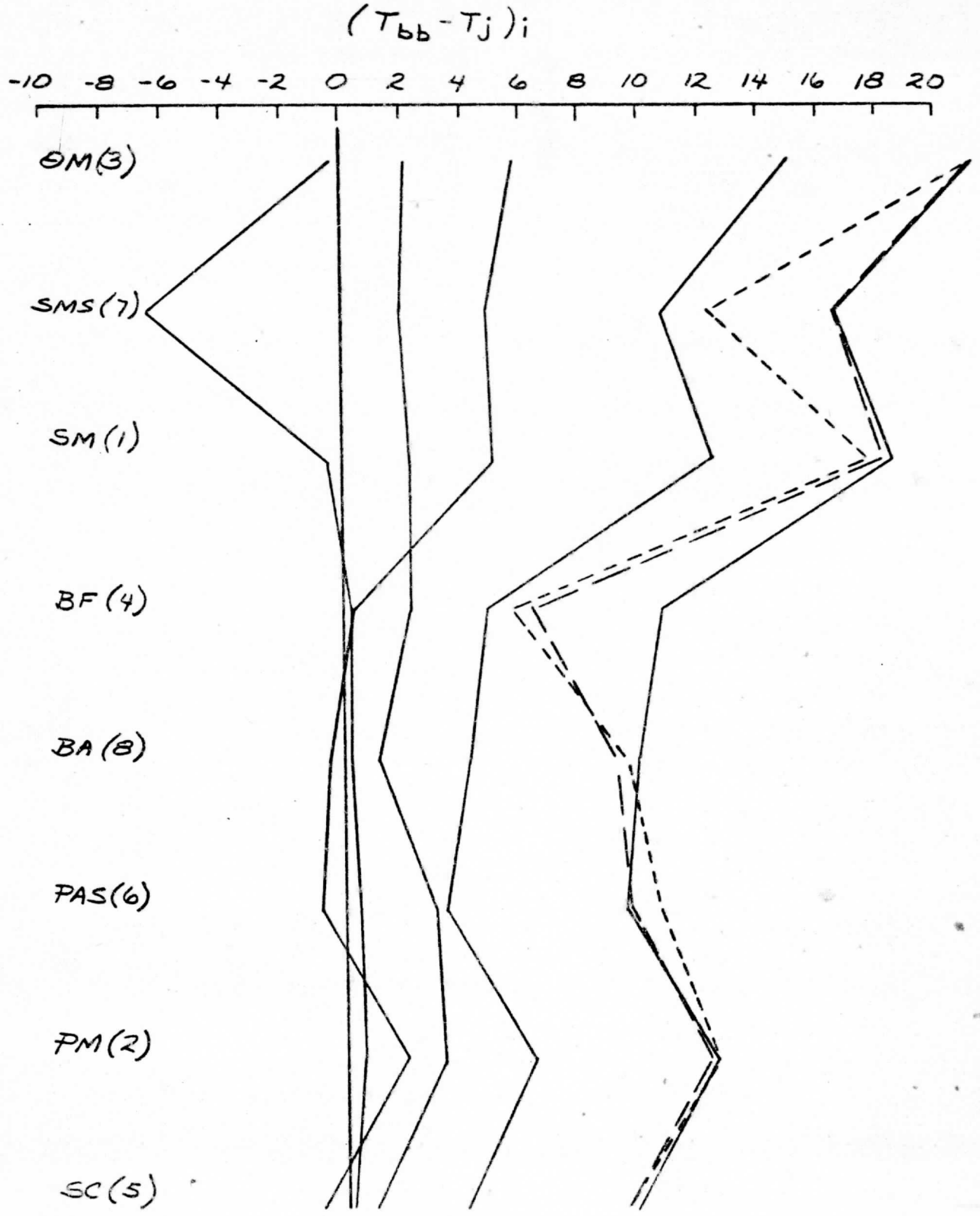

FIGURE I.3 VAS-D THERMAL GRADIENTS PRODUCED IN CALIBRATION AND ACCEPTANCE TEST

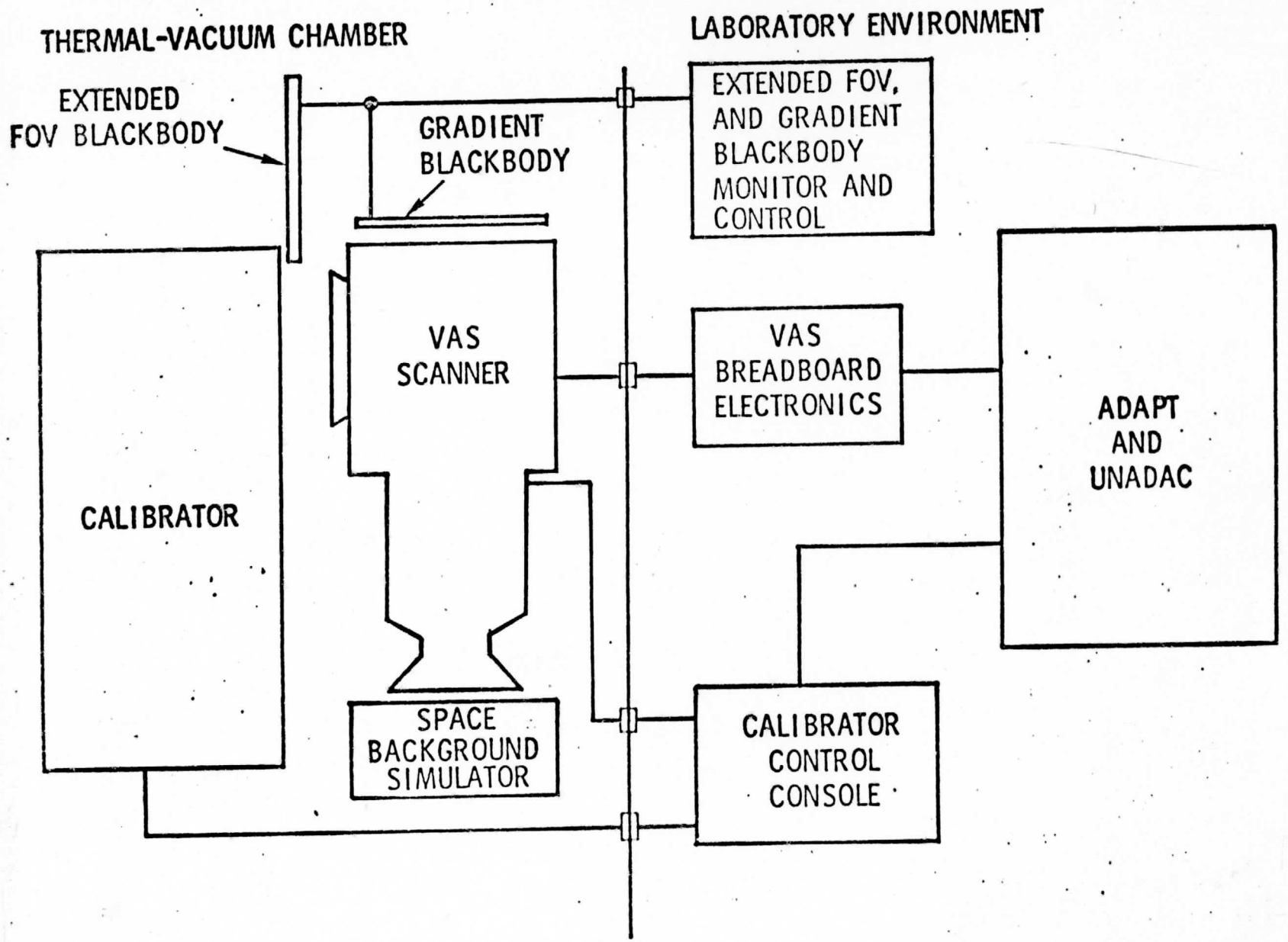

Figure I.4 Thermal Vacuum Test Configuration

To evaluate the effective blackbody radiance external to VAS

$$N_{BV} = R_{bb} + \sum_{i=1}^{8} c_i \, (R_{bb} - R(T_i)) \qquad (I.21)$$

and the effective blackbody radiance external to the calibrator

$$N_{BC} = N_{BV} + \sum_{i=9}^{10} c_i (N_{BV} - R(T_i)) \qquad (I.22)$$

where $C_9 = .110$ accounts for CM and $C_{10} = .010$ for 5PM. Thus, the algorithm determined external target radiance,

$$N_T^A = \frac{V_T - V_Z}{V_I - V_Z} N_{BC}, \qquad (I.23)$$

can be compared to the measured external target radiance

$$N_T^M = R(T_{ET}). \qquad (I.24)$$

With the coefficients determined from the ray tracing, the absolute error and relative error of $(N_T^A - N_T^M)$ for the 28 test gradients for band 8 were calculated to be $-.77 \pm .71$ ergs/etc. (or $-.46 \pm .41^{o}C$). While this result is within specifications, improved results were sought by changing C_{BF} and C_{SMS}. The thermal gradients were sufficiently uncorrelated to determine C_{BF} and C_{SMS} from the test data explicity. Using an analysis of covariance (see Appendix C), C_{BF} was found to change from .168 to .129 and C_{SMS} from .228 to .195 for band 8. The errors were thus changed to $-1.56 \pm .24$ ergs/etc. (or $.92 \pm .14^{o}C$), which improves the relative error significantly while degrading the absolute error.

Performing the same analysis many times with normally distributed random noise added on to the individual measurements (thermistor readings are accurate to $.1^{o}C$ and voltage measurements are accurate to .005 volts) allows a determination of an accuracy estimate of the two coefficients. From 100 noise runs, $C_{BF} = .129 \pm .058$ and $C_{SMS} = .195 \pm .022$. The ranges of these estimates overlap with the ranges of the ray trace estimates.

The uncertainty of the effective external blackbody radiance determination can be expressed in terms of the uncertainties in the calibration coefficients and the expected inflight foreoptics radiance gradients,

$$\Delta N_B = \{\Sigma_i \Delta C_i^2 [R(T_{bb}) - R(T_i)]^2\}^{1/2}. \qquad (I.25)$$

Figure I.5 shows the expected inflight thermal gradients for summer, winter, and equinox. The corresponding ΔN_B are .15 erg/etc., .10 erg/etc., and .05 erg/etc., respectively.

In an effort to explain the rather large absolute error, the detector nonlinearity was incorporated explicitly into equations (I.5) through (I.7) so that they become

$$(1-\gamma)N_V = a + bV_Z + cV_Z^2, \qquad (I.5')$$

$$N_I = a + bV_I + cV_I^2, \qquad (I.6')$$

$$\gamma N_T + (1-\gamma)N_V = a + bV_T + cV_T^2. \qquad (I.7')$$

Using the identity

$$\gamma N_B + (1-\gamma)N_V = N_I, \qquad (I.25)$$

and proceeding as before, we find

$$N_T = N_B \left\{\frac{b(V_T-V_Z) + c(V_T^2 - V_Z^2)}{b(V_I-V_Z) + c(V_I^2 - V_Z^2)}\right\}. \qquad (I.26)$$

Inserting the band 8 nonlinearity of c/b = .002 did not change the previous results noticeably. The explanation for the large absolute error must lie elsewhere.

Similar results and conclusions were ascertained for the remaining 11 spectral bands of VAS-D. The results are tabulated in Table I.2.

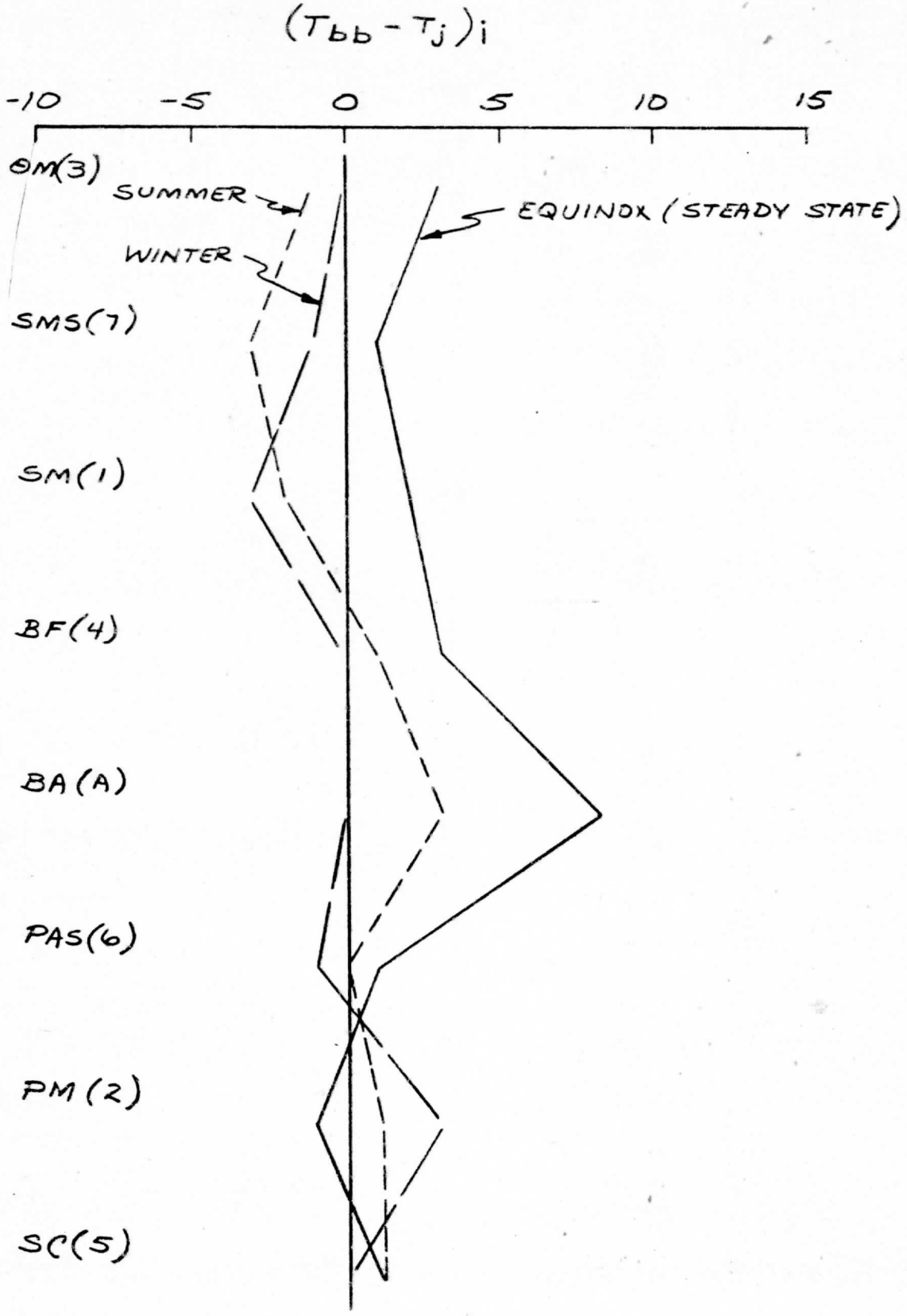

FIGURE I.5. VAS D THERMAL GRADIANTS EXPECTED IN SPACE

Table I.2 VAS-D Calibration Coefficients

Band	C_{BF}	C_{SMS}	abs. error (in ergs/etc.)	rel. error
1	.145 ± .058	.153 ± .022	- .46	.73
2	.118	.133	-1.05	.54
3	.133	.142	-1.07	.29
4	.118	.141	-1.27	.46
5	.131	.157	-1.34	.38
6	.133	.155	- .06	.02
7	.145	.178	-1.33	.27
8	.129	.195	-1.56	.24
9	.125	.228	- .44	.23
10	.173	.198	- .38	.14
11	.128	.179	- .05	.01
12	.152	.214	- .02	.01

The remaining calibration coefficients remain at their ray trace value (see Table I.1). Absolute and relative errors are determined for the 28 gradients produced in the Calibration and Acceptance Test.

Conclusions

The following conclusions can be inferred from the test results.

(1) Using the ray trace coefficients to determine the absolute and relative error for the 28 test gradients yields results within the specifications.

(2) The test gradients were sufficiently uncorrelated to allow unique determination of the coefficients of the two largest contributors to the background radiation, C_{SMS} and C_{BF}.

(3) Using this combination of ray trace and test determined coefficients, improved relative errors with respect to the test data were obtained.

(4) The uncertainty of the effective external blackbody radiance determination ranges from .05 erg/etc. to .15 erg/etc. during the year for band 8. Comparable results for the other bands were also found.

(5) The rather large absolute errors cannot be explained by detector nonlinearities. For band 8, the small nonlinearity did not change the results; for the other bands the nonlinearity was negligible.

Operational Implementation

The implementation of the calibration algorithm in the VAS Synchronizer Data Buffer is accomplished with a five-step procedure. A brief outline follows.

(1) Determine temperature of VAS-D telescope foreoptics components from thermistor digital readings S_i

$$T_i = \sum_{j=0}^{3} a_{ij} S_i^j,$$

where i is the component index and the a_{ij} are determined from curve fitting.

(2) Extract radiances of telescope components for the different spectral band-detector combinations (there are 38 in all) from the temperatures

$$R_{ki} = \sum_{j=0}^{3} b_{kj} T_i^j$$

where k is the band-detector index, and the b_{kj} comes from polynomial fits of the radiance integrated over spectral response (see equation I.15).

(3) Use the calibration algorithm to determine an equivalent external blackbody radiance for the band-detector combination

$$N_k^B = R_{k,bb} + \sum_{j=i}^{8} c_{kj}(R_{k,bb} - R_{kj}).$$

(4) Correct the detector response for detector nonlinearities to generate a computed signal X for space, target, and internal blackbody views.

$$X_k = \sum_{j=0}^{3} d_{kj} D_k^j.$$

(5) Calculate the target radiance

$$N_k^T = \left[\frac{N_k^B}{X_k^B - X_k^Z}\right] X_k^T - \left[\frac{N_k^B X_k^Z}{X_k^B - X_k^Z}\right].$$

II. VAS DETECTOR NOISE REDUCTION ANALYSIS

Temperature soundings of the atmosphere can be made with VAS only if clear column spectral radiances over the initial regions of interest are determined within a standard error of .25 erg/(sec-ster-cm^2-cm^{-1}). Instrumentation specified for sounding with VAS can achieve this only by averaging many individual measurements, each with a standard error larger than that required for successful sounding. Therefore, it is necessary to understand precisely the effectiveness of such averaging procedures in reducing detector noise.

The Effect of Noise Correlation

If all the radiance measurements contained only random independent noise, then the standard error of the mean of N measurements, each with standard error σ, would just be the familiar $\sigma/\sqrt{N}$. However, the infrared detectors on VAS have substantial amounts of low frequency noise so that samples taken at higher frequency will experience noise contributions with significant correlation. This implies that the standard of error of the average of N VAS IR measurements will be larger than $\sigma/\sqrt{N}$. To determine how much larger, consider the expected variance of the means of samples of size N

$$\sigma_M^2 = E[(M-\mu)^2] = E(M^2) - \mu^2 \qquad \text{(II.1)}$$

where μ is the population mean (assumed to be zero for simplicity), and M is the mean of N detector noise voltage samples, $e(t_i)$, which we write as

$$M = \frac{1}{N} \sum_{i=1}^{N} e(t_i), \qquad \text{(II.2)}$$

and E denotes the expectation value

$$E[e(t)e(t+\tau)] = \lim_{T\to\infty} \frac{1}{T} \int_{-\frac{T}{2}}^{+\frac{T}{2}} e(t)e(t+\tau)dt \qquad \text{(II.3)}$$

which is just the autocovariance function $C(\tau)$. Then we can write

$$\sigma_M^2 = \frac{1}{N^2} \sum_{i=1}^{N} \sum_{j=1}^{N} E[e(t_i)e(t_j)]$$

$$= \frac{1}{N^2} \sum_{i=1}^{N} \sum_{j=1}^{N} C(t_j - t_i). \qquad \text{(II.4)}$$

But the signal variance is defined as

$$\sigma^2 = \lim_{T\to\infty} \frac{1}{T} \int_{-\frac{T}{2}}^{+\frac{T}{2}} [e(t)]^2 dt$$

$$= C(0), \qquad \text{(II.5)}$$

so we have

$$\sigma_M^2 = \frac{\sigma^2}{N} + \frac{1}{N^2} \sum_{i=1}^{N} \sum_{j\neq 1}^{N} C(t_j - t_i). \qquad \text{(II.6)}$$

This shows explicitly the effect of noise correlation. If $e(t_i)$ and $e(t_j)$ were random independent variables, then we would have $C(t_j - t_i) = 0$ for $i \neq j$ and $\sigma_M^2 = \sigma^2/N$. Since $e(t_i)$ and $e(t_j)$ are correlated, a considerably different result is obtained.

The variance of the means of the VAS data samples has been determined from a theoretical model of the detector electronics and from pre-launch raw VAS data explicitly. Both sets of results will be presented in the following pages; first the theoretical results and then the actual pre-launch performance.

Theoretical Evaluation of Noise Characteristics

To evaluate the variance of the means of many detector samples, one must represent the spectral distribution of the detector noise power and the spatial distribution of the samples to be averaged. For the purposes of this discussion, the detector noise can be completely described by the noise power spectral density

$$P(f) = \lim_{T\to\infty} \frac{2}{T} \left| \int_{-\frac{T}{2}}^{+\frac{T}{2}} e(t)\exp(-2\pi ft)\,dt \right|, \qquad \text{(II.7)}$$

where f is frequency, and the autocovariance function is given by

$$C(\tau) = \lim_{T\to\infty} \frac{1}{T} \int_{-\frac{T}{2}}^{+\frac{T}{2}} e(t)e(t+\tau)\,dt. \qquad \text{(II.8)}$$

The two functions can be related through a cosine transform

$$C(\tau) = \int_0^\infty P(f)\cos(2\pi f\tau)\,df, \qquad \text{(II.9)}$$

implying that the signal variance can be written

$$\sigma^2 = C(0) = \int_0^\infty P(f)\,df. \qquad \text{(II.10)}$$

P(f)df represents the contribution to the signal variance from frequencies between f and f + df.

P(f) appropriate to the VAS detector comes from two independent processes. The generation-recombination noise which is independent of frequency and the 1/f noise. The frequency at which these two are equal, f_c, is called the crossover frequency. Filtering the detector signal to eliminate all frequencies below f_{min} and above f_{max} yields an effective noise power spectrum

$$P(f) = \sigma^2(1 + f_c/f)/\Delta f_n \qquad f_{min} \leq f \leq f_{max}$$

$$= 0 \quad \text{otherwise,}$$

where the noise equivalent bandwidth

$$\Delta f_n = f_{max} - f_{min} + f_c \ln(f_{max}/f_{min}). \tag{II.11}$$

Including the power transfer function of the electronic filter, T(f), the autocovariance reads

$$C(\tau) = \int_0^\infty T(f)P(f)\cos(2\pi f\tau)df. \tag{II.9'}$$

T(f) is evaluated as the product of the power transfer function of the presampling filter (modeled to be a 5 pole Bessel filter) and the power transfer function of the DC restore circuit (which behaves like an RC circuit).

The transfer function for a 5 pole low pass (LP) Bessel filter can be written

$$T_{LP}(f_{LP}) = 945/[(945-420f_{LP}^2 + 15f_{LP}^4)^2 + (945f_{LP} - 105f_{LP}^3 + f_{LP}^5)^2]^{1/2},$$

where f_{LP} is the low pass frequency. To translate this into a band pass filter transfer function, scale to band pass frequencies as follows

$$\frac{f_{LP}}{f_{max,LP}} = \frac{f_0}{f_{max} - f_{min}} \left[\frac{f}{f_0} - \frac{f_0}{f}\right]$$

where $f_0 = \sqrt{f_{max} f_{min}}$, and write

$$T_{BP}(f) = T_{LP}(f_{LP}). \tag{II.12}$$

The VAS DC restore noise transfer function can be written

$$T_{DCR}(f) = 1 + \frac{1}{1 + (2\pi fT_2)^2} - \frac{2}{(2\pi fT_1)\sqrt{1 + (2\pi fT_2)^2}} \times [\sin(2\pi fT_1 - \theta) + \sin\theta] \tag{II.13}$$

where T_1 is the data gathering time, T_2 is the time constant of the RC circuit, and $\theta = \arctan(2\pi f T_2)$. The effective power transfer function is the product

$$T(f) = T_{BP}(f)T_{DCR}(f). \qquad \text{(II.14)}$$

Figure II.1 shows a plot of T(f) evaluated for f_{min} = .026 Hz, f_{max} = 26 KHz, T_1 = 30 msec, and T_2 = 10 msec. The oscillatory behavior of the transfer function near the low pass edge is due to the DC restore circuitry. Figure II.2 shows a plot of the autocovariance $C(\tau)$ evaluated for the large HgCdTe detector (f_c = 750 Hz) and the InSb detector (f_c = 10 Hz) with a sampling interval of 8 μsec. Figure II.3 shows plots of σ_M^2/σ^2 as a function of N, the number of samples for both HgCdTe and InSb detectors. Averaging means from more than 10 contiguous samples shows the 1/N behavior expected since the autocovariance has dropped off appreciably.

Analysis of Noise Reduction from Test Data

Evaluation of the autocovariance function from raw data produced during the Calibration and Acceptance Test (September 1979) indicated that there is less autocovariance than expected. Therefore, σ_M^2/σ^2 reduces more rapidly as a function of sample number. Figures II.4 and II.5 show the plots of $C(\tau)$ and σ_M^2/σ^2 for large HgCdTe band 8 data (11.2 micron) and large InSb band 12 data (3.9 micron). Plots for the remaining ten spectral bands are comparable.

It now remains to evaluate a spin budget. Table II.1 shows the spin budget evaluated for the upper large detectors (Channel 1) and the lower large detectors (Channel 2). The conversion from σ, the single sample noise, to σ_M, the noise of the mean of several samples needs explanation. For band 1, samples from 150 x 150 km^2 at the subsatellite point are averaged: this represents 46 samples of correlated noise per

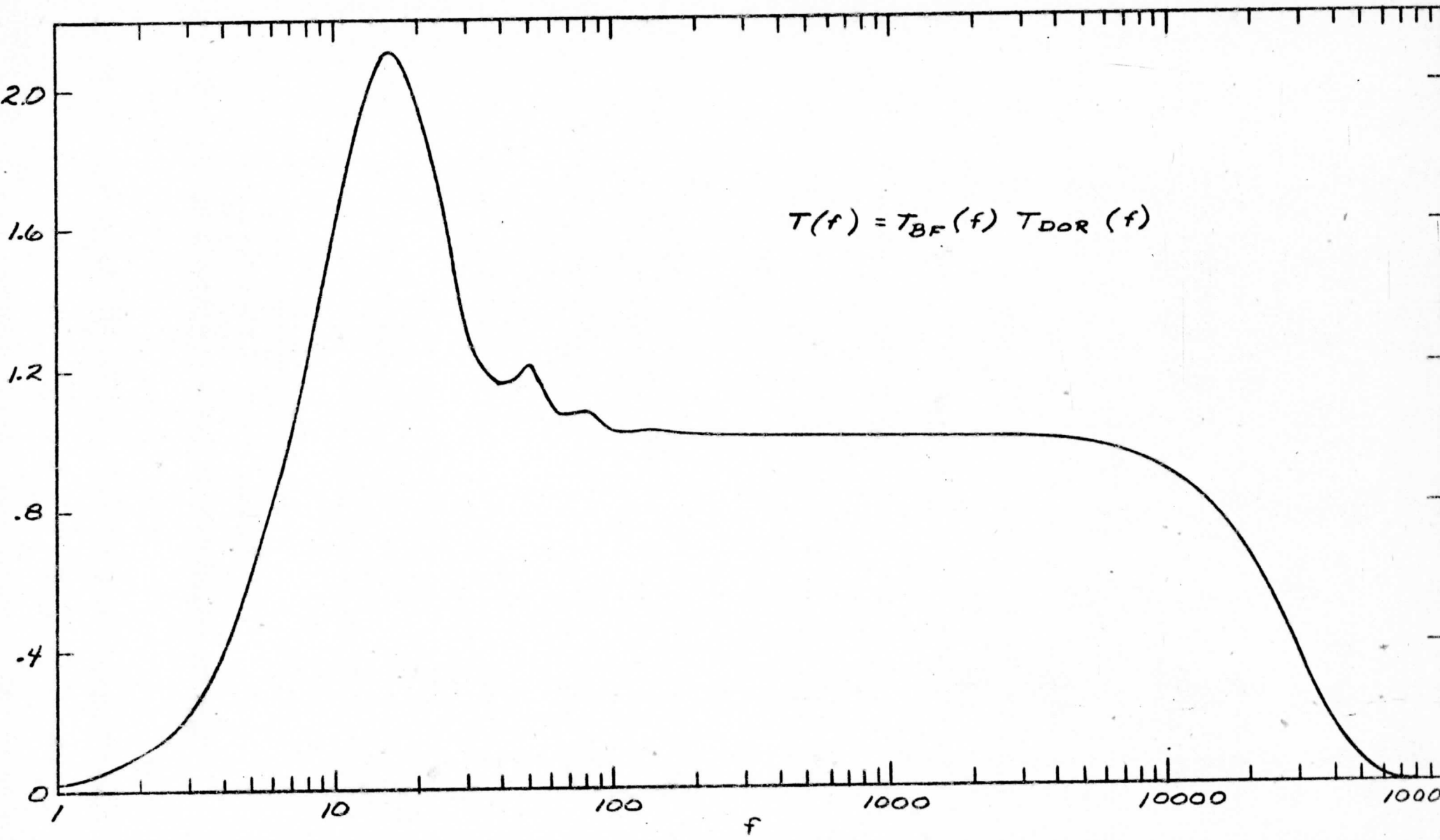

FIGURE II. 1. VAS POWER TRANSFER FUNCTION

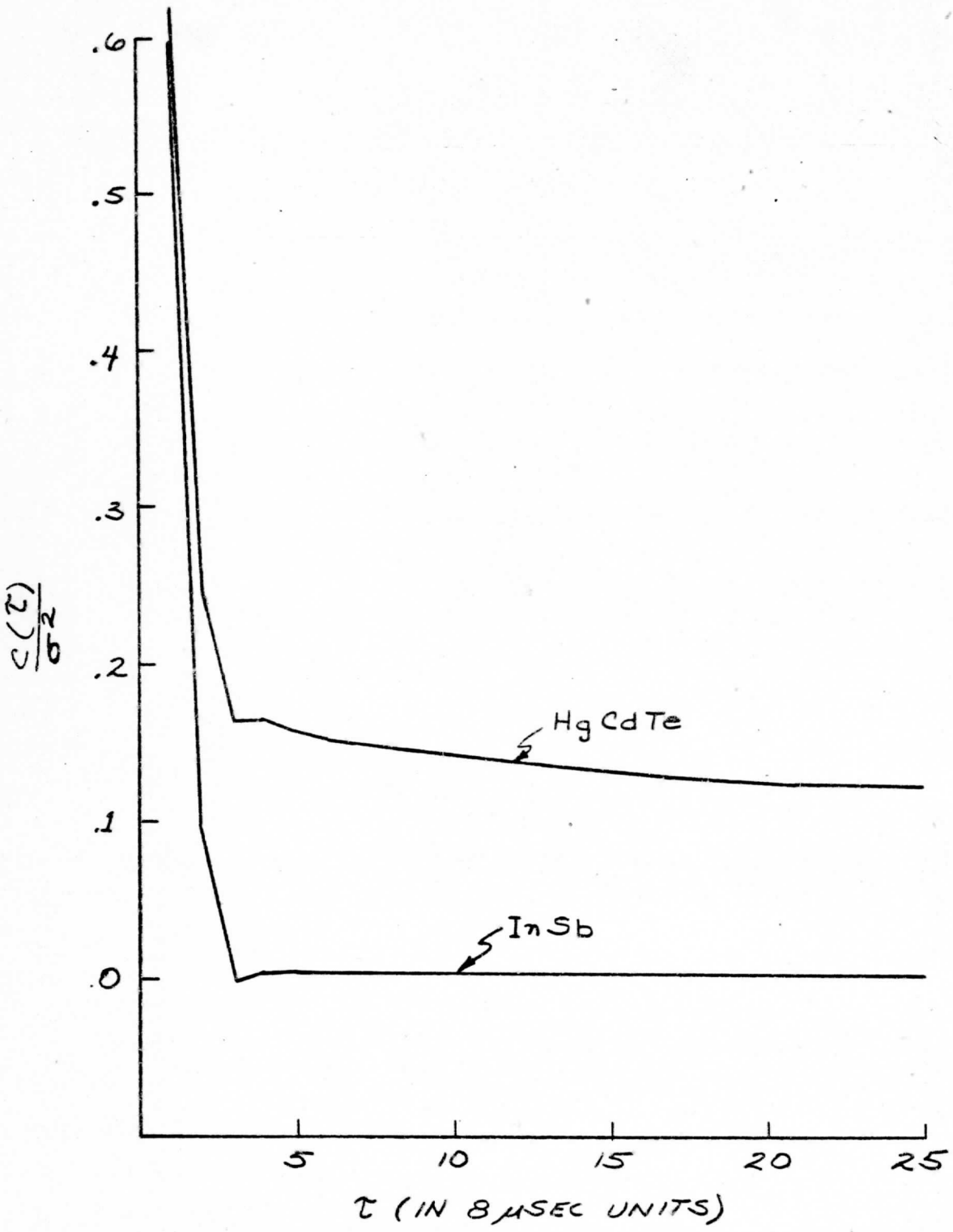

FIGURE II. 2 AUTOCOVARIANCE OF NOISE $C(\tau)/\sigma^2$ AS A FUNCTION OF SAMPLING INTERVAL τ IN LARGE DETECTORS EVALUATED FROM NOISE MODEL

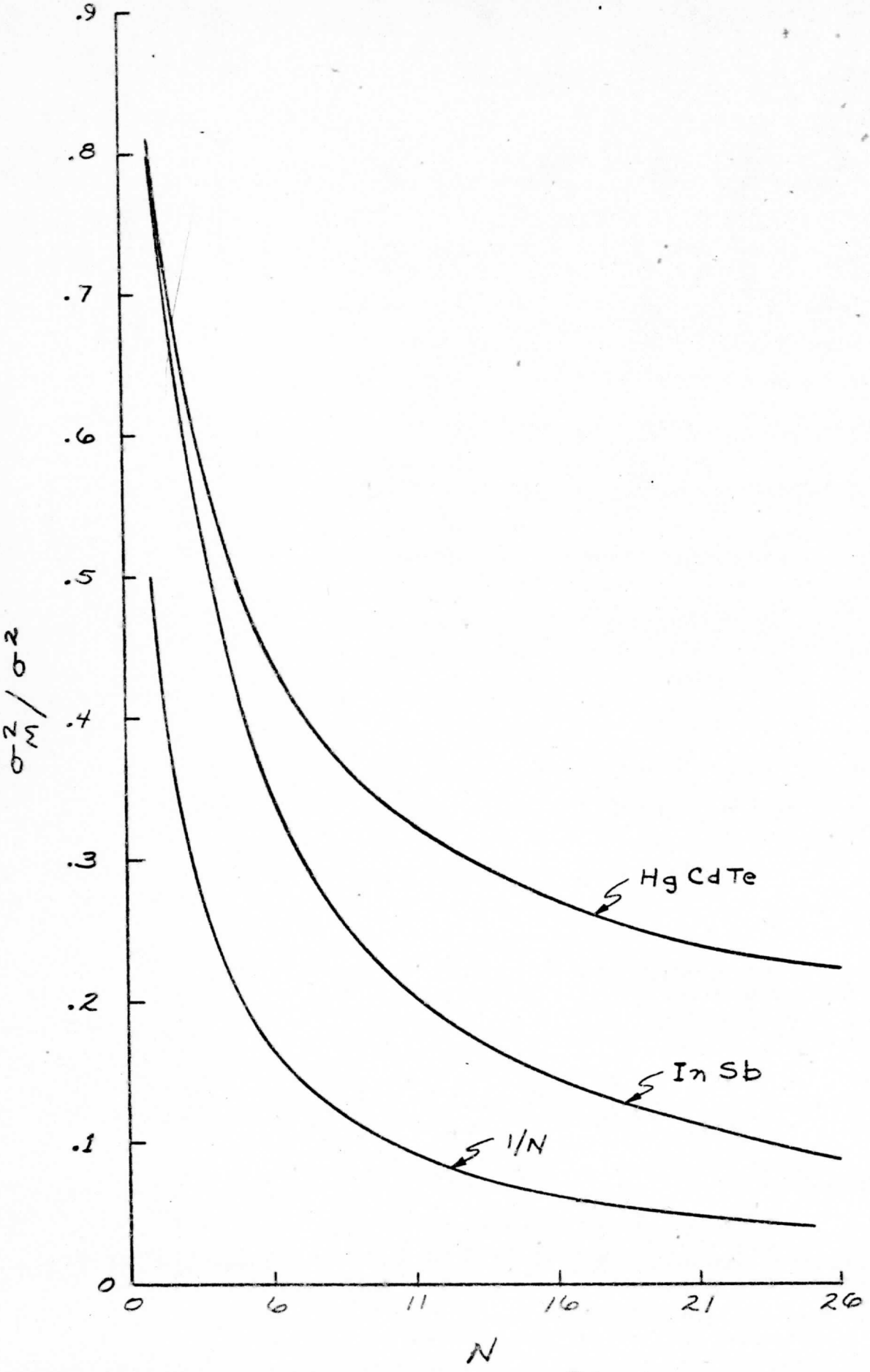

FIGURE II.3. THEORETICAL σ_m^2/σ^2 AS A FUNCTION OF SAMPLES N FOR CORRELATED NOISE ON ONE SPIN. 1/N CURVE REPRESENTS UNCORRELATED NOISE.

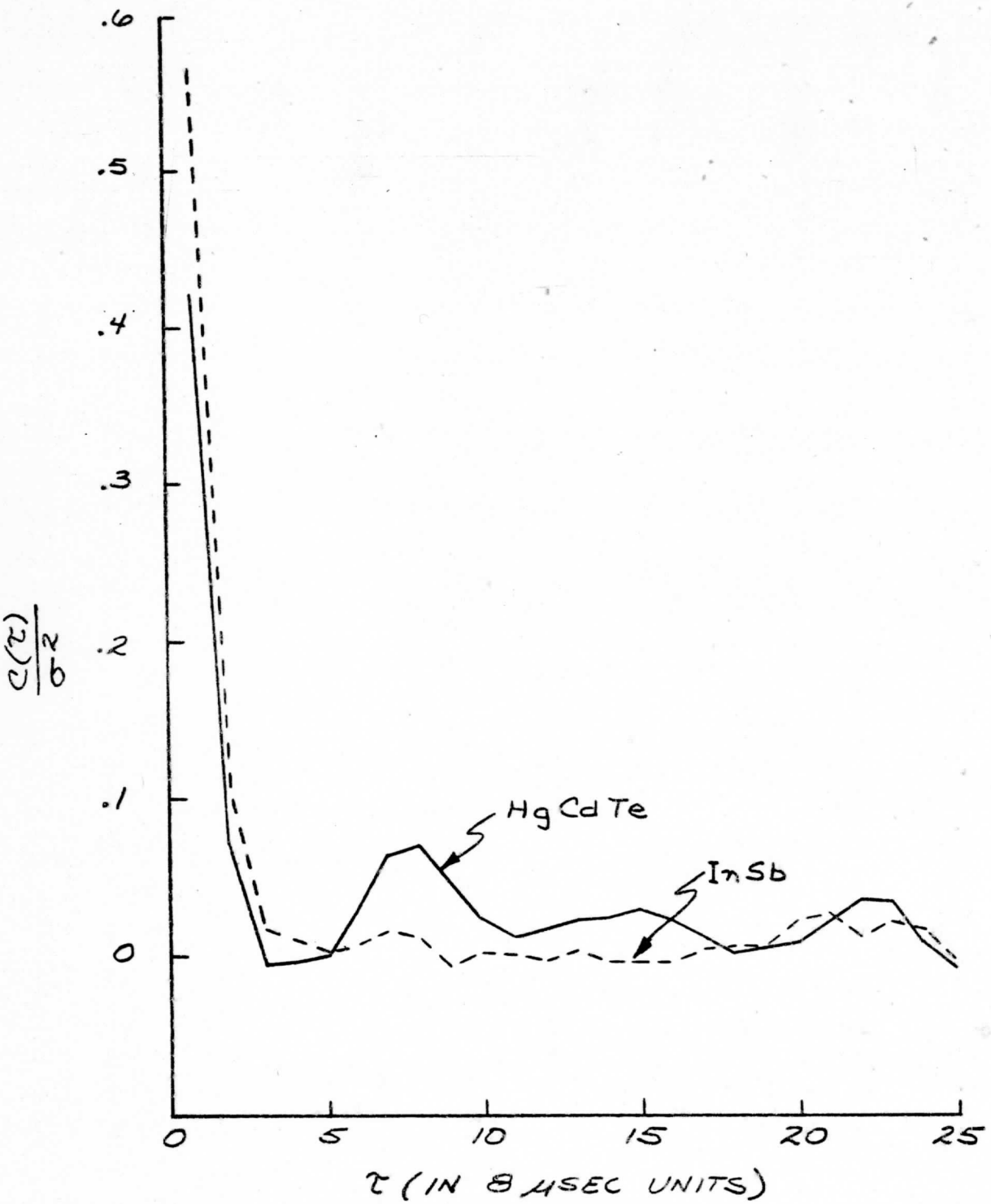

FIGURE II. 4 AUTOCOVARIANCE OF NOISE $C(\tau)/\sigma^2$ AS A FUNCTION OF SAMPLING INTERVAL τ DETECTORS EVALUATED FROM CALIBRATION ACCEPTANCE TEST DATA.

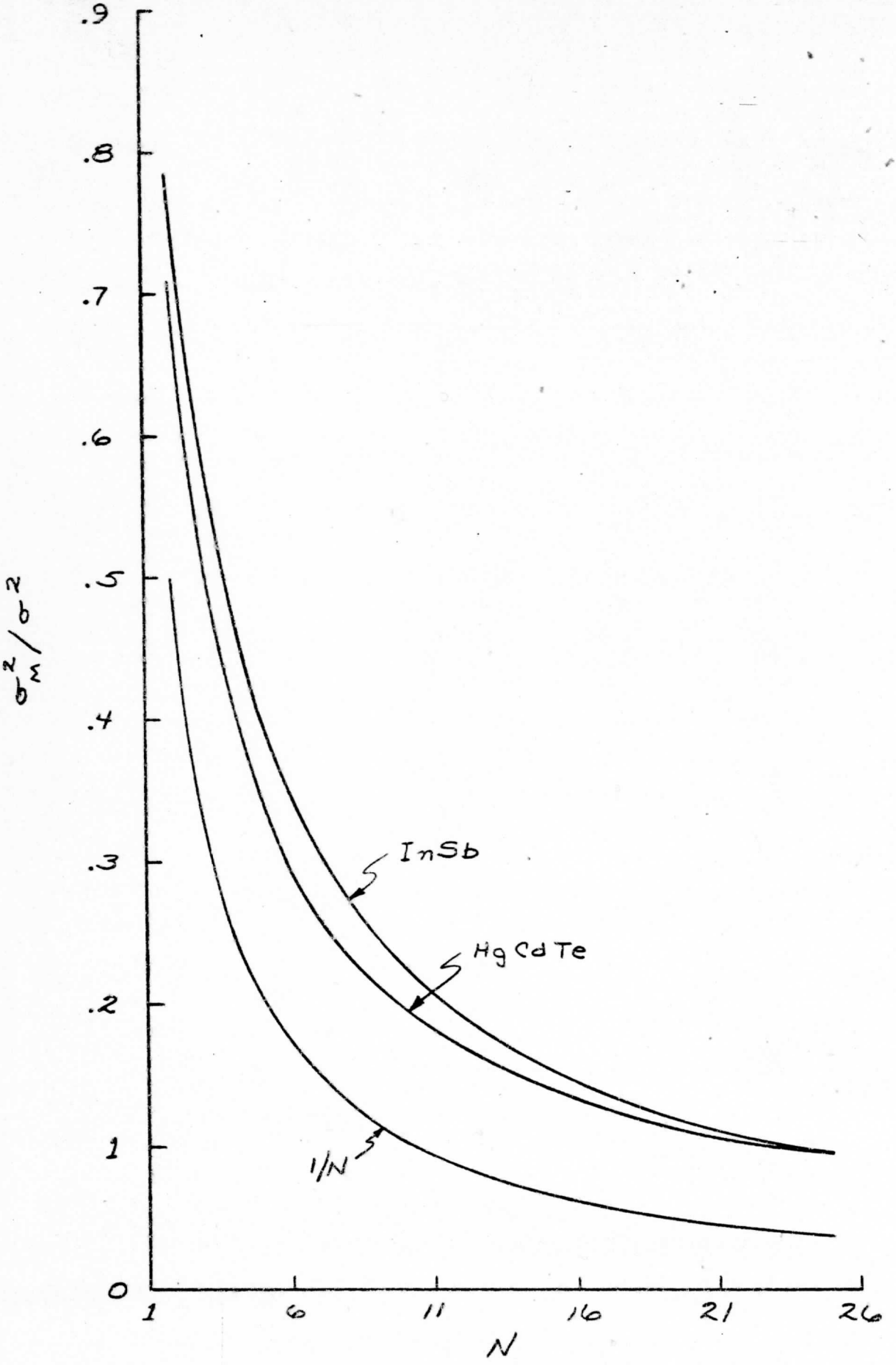

FIGURE II.5. σ_M^2/σ^2 AS A FUNCTION OF THE NUMBER OF SAMPLES N EVALUATED FROM CALIBRATION ACCEPTANCE TEST DATA.

Table II.1 VAS D Large Detector Spin Budget

Band	σ(erg/etc)	I	σ_M (erg/etc)	σ_{Req} (erg/etc)	Spin Budget
1U†	4.90	12.88*	.38	.25	3
1L	4.34	13.52*	.32	.25	2
2U	2.99	2.49	1.20	.25	23
2L	2.87	2.67	1.07	.25	19
3U	2.11	2.54	.83	.25	11
3L	1.57	2.46	.64	.25	7
4U	1.94	2.54	.76	.25	10
4L	1.55	2.52	.62	.25	7
5U	1.32	2.57	.51	.25	5
5L	1.17	2.53	.46	.25	4
6U	.024	2.37	.010	.004	7
6L	.025	2.39	.010	.004	7
7U	1.15	2.58	.45	.25	4
7L	.88	2.41	.37	.25	3
8U	.15	2.60	.06	.25	1
8L	.12	2.32	.05	.25	1
9U	1.41	2.56	.55	.15	14
9L	1.22	2.82	.43	.15	9
10U	.28	2.38	.13	.10	2
10L	.29	2.55	.11	.10	2
11U	.023	2.39	.009	.004	6
11L	.024	2.39	.010	.004	7
12U	.007	2.38	.003	.004	1
12L	.007	2.37	.003	.004	1
Total U					87
L					69

*Improvement factor for band 1 is evaluated for samples from 150 x 150 km^2; for all other bands it is evaluated for samples from 30 x 30 km^2.

†U indicates upper, L indicates lower.

spin for 10 independent spins. For the remaining bands, samples from 30×30 km^2 are averaged: this involves 6 correlated noise samples per spin for 2 spins. The noise is uncorrelated from one spin to the next. The conversion from σ to σ_M is accomplished by the noise improvement factor, I, defined so $\sigma_M = \sigma/I$. I is evaluated from the raw data explicitly. The number of spins to achieve the required noise level is derived assuming $1/\sqrt{N}$ reduction in noise by multiple spins over the same area. Table II.1 shows that the performance of the lower large detectors is markedly improved over that of the upper large detectors. Table II.2 shows the spin budget for the small HdCdTe detectors (upper and lower) when sounding for 15×15 km^2 is desired: this involves 3 correlated noise samples per spin for 2 spins. Again, we find that the lower small detector performance is superior to that of the upper small detector.

With a spin budget of 87, assuming the spacecraft rotation of 100 rpm, the sounding rate at subsatellite point is roughly 30 km/min for continguous coverage. Appendix A describes the sounding rates in more detail. Note that to achieve the desired signal to noise in both detectors simultaneously the larger of the upper and lower detector spin budgets must be adopted.

Conclusions

From these noise reduction tests we infer the following conclusions.

(1) The effects of correlated noise on signal to noise enhancement are understood well enough to estimate reliable spin budgets.

(2) The autoconvariance of noise found in the HgCdTe detectors is appreciably smaller than predicted.

Table II.2 VAS D Small Detector Spin Budget

Band	σ(erg/etc)	I*	σ_m(erg/tec)	σ_{Req} (erg/etc)	Spin Budget
3U†	4.55	1.80	2.52	.25	102
3L	3.94	1.86	2.12	.25	72
4U	4.39	1.85	2.37	.25	90
4L	3.62	1.85	1.96	.25	62
5U	2.92	1.80	1.58	.25	40
5L	2.84	1.88	1.51	.25	37
7U	2.69	1.81	1.49	.25	36
7L	2.40	1.91	1.26	.25	26
8U	.35	1.77	.20	.25	1
8L	.32	1.82	.18	.25	1
9U	3.26	1.80	1.81	.15	146
9L	3.03	1.88	1.61	.15	116
10U	.77	1.78	.43	.10	19
10L	.73	1.86	.39	.10	16
Total U					434
L					330

*Improvement factors for all bands are evaluated for samples from 15 x 15 km^2.

†U indicates upper, L indicates lower.

(3) The performance of the lower HgCdTe detectors is 25% more efficient in signal to noise enhancement than that of the upper HgCdTe detectors.

(4) Using both upper and lower large detectors, with a spin budget of 87, the VAS-D can dwell sound a 60 km swath at 30 km^2 resolution (except for band 1) over the United States in 110 sec. Sounding with the small detectors at 15 km^2 resolution takes roughly five times as long.

III. EFFECT OF REGISTRATION ERRORS AND DIFFRACTION ON CLEAR COLUMN RADIANCE RETRIEVALS

Several of the retrieval techniques considered for obtaining clear column radiances from cloudy scenes require that the spatial weighting of the scene within each FOV be identical for different spectral bands. A number of registration errors have been identified which make it impossible to achieve this ideal of identical spatial weighting. The effect of registration errors on sounding band radiance retrievals has been studied by numerical simulation of the measurements and the retrieval algorithms. The results are discussed in this report. Also, although the errors in window band clear column retrievals caused by diffraction are not registration errors, they are discussed here because of their importance to sounding band retrievals.

Clear Column Radiance Retrieval: An Explanation of One Method

The technique used in these studies for clear column radiance retrieval (CCRR) is the Paired Field of View (PFOV) procedure. The PFOV procedure utilizes the fact that from a single FOV partially filled with clouds of a single type the radiance of one frequency is linearly related to the radiance of another frequency. Thus, a plot of radiance measurements from a window band clear column radiance (see Fig. III.1). The PFOV procedure assumes that for a given pair the sounding and window band radiances come from the same geometric FOV. If the sounding FOV is misregistered from the window FOV, then errors are introduced into the sounding clear column radiance retrieval (CCRR).

Causes for Misregistration

The registration of fields of view (FOV) of different spectral bands using the same detector is complicated by

(1) line start timing errors,

(2) errors in the equal angle (EA) resampling of spacecraft equal time (ET) samples,

(3) subsatellite point motion (apparent earth motion) due to orbit eccentricity and inclination to the equatorial plane,

(4) location errors due to nutation of the satellite spin axis,

(5) location errors due to motion of the scene,

(6) alignment problems due to filter cocking, and

(7) diffraction variations with wavelength.

The line start error in the VAS Line Stretcher timing system can be summarized as follows: the jitter of the sun pulse output (peak value = .425 μsec) and the quantization of the Digital Phase Lock Loop (peak value = .1 μsec) combine for a line start timing error peak value of .53 μsec (1.4% of large detector FOV).

The VAS EA resampling system has two steps: first augment the ET samples with one sixteenth interval values determined by a three point Lagrangian interpolation, and then set the EA value to be that of the nearest ET radiance measurements (actual or interpolated). A simulation of EA resampling of ET radiance measurements (real detector response to scene that has 100 ergs/etc jump) produced peak errors of .49 μsec (1.3% of large detector FOV).

Paired Field of View (PFOV) Technique

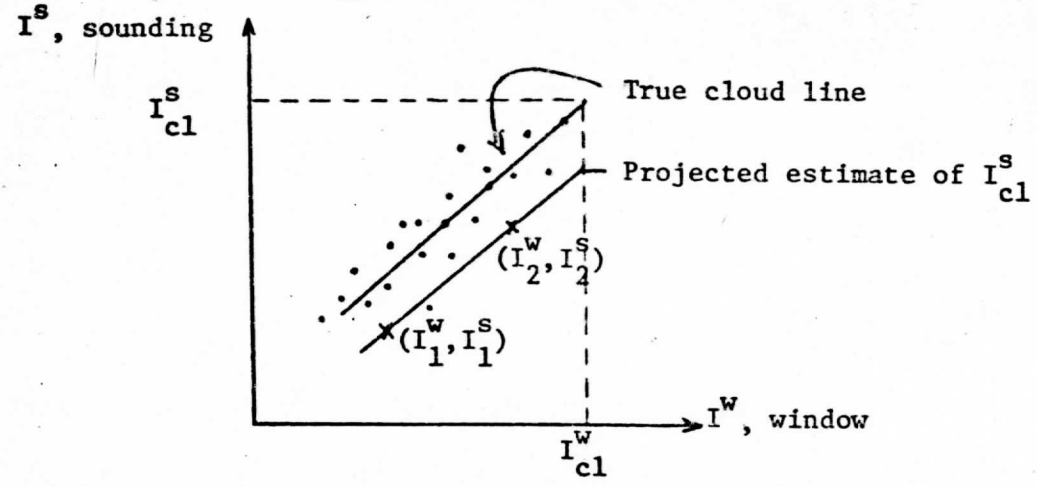

$$I^s_{cl} = \frac{I^s_1 - N^* I^s_2}{1 - N^*}$$

where

$$N^* = \frac{I^w_1 - I^w_{cl}}{I^w_2 - I^w_{cl}} = \text{ratio of cloud covers for two FOV's}$$

I^w_1, I^w_2 = window band radiance measurements from two fields of view

I^s_1, I^s_2 = corresponding sounding band radiance measurements.

I^w_{cl} = known window clear column radiance

I^s_{cl} = calculated sounding clear column radiance

Figure III.1

Errors due to (1) and (2) occur randomly in each spin scan and can be reduced for any band by multiple scanning. Ten scans would reduce the errors by a factor of $1/\sqrt{10}$.

Satellite orbital eccentricity and inclination with respect to the equatorial plane causes a twenty-four hour periodic sub-satellite point motion that can be expected to be as large as 2° latitude (roughly 450 km north-south) and 1/2° longitude (roughly 50 km east-west). These periodic displacements correspond to a speed of roughly 60 km/hr for the path of the detector FOV on the earth surface. If there is a time interval of 30 seconds between the window band and the more cloud sensitive sounding bands, then misalignments as large as .014 mrad (3.5% of a large detector FOV) are possible between the window band and some sounding bands. For any given sounding band this error depends on the order in which the bands are sampled; 30 sec is representative of the time between window band 8 and sounding band 5.

Nutation of the S/C spin axis is caused in part by the scan mirror motion, SEM motion, and control jets. A passive damper reduces nutation amplitudes to .5 arc sec in times dependent on the magnitude of the induced nutation. The period of nutation is roughly 6 sec, so that maximum window and sounding band misalignments due to nutation are .005 mrad (1.3% of large detector FOV).

Location errors are also caused by motions of the scene. A cloud at sub-satellite point with a speed of 30 km/hr can cause a maximum window to sounding band misalignment of .007 mrad (1.8% of large detector FOV) in half a minute of sounding.

These errors (3), (4) and (5) can be reduced for a given sounding band if the time between the window band scan and sounding band

scans is reduced. Errors (3) and (5) could be halved if the time between window scans were halved.

The band to band registration of FOVs using the same detector are also affected by a cocking of the twelve filters with respect to one another. The resulting east-west shifting can be corrected, while the north-south misregistration cannot. Nominal pointing changes in the north-south direction due to filter changes are roughly .004 mrad (1.1% of a large detector FOV).

The effect of variations of diffraction with wavelength and the basis of the diffraction calculations are discussed in Appendix B. The diffractive function is incorporated into the spatial weighting function and cannot be described as a misregistration of a percentage of a FOV.

The registration of FOVs of different spectral bands using different detectors is affected by all of the previously cited problems plus

(1) position errors in detector array fabrications,

(2) alignment problems because the VAS optical axis is not identical with the spacecraft spin axis,

(3) responsivity variations across the detector surfaces, and

(4) differences in the effective size of the detectors due to blur variations with field angle.

The effects of the first two problems can be summarized together. The centers of the large HgCdTe and the large InSb detectors are displaced by less than .015 mrad in the north-south direction. The VAS telescope axis is within 5 mrad of the spacecraft spin axis. The combined effect introduces a .020 mrad (5.2% of a large detector FOV) misregistration between the large HgCdTe and InSb detectors.

The effective size of the large detectors differs appreciably due to blur variations with field angle. Santa Barbara Research Center measured the relative locations of the VAS-D infrared FOV centers and their east-west and north-south widths. This information is summarized in the Calibration and Performance VAS-D/GOES Data Book. On the average, the large HgCdTe are .315 mrad N/S by .400 mrad E/W and the InSb are .424 mrad N/S by .426 mrad E/W. This difference in the detector sizes is incorporated in the spatial weighting functions.

The responsivity of the detector varies across the surface. The peak to peak drop-off for the large detectors ranged from 5% to 15% in the east-west direction and was 5% in the north-south direction. These effects are also included in the spatial weighting functions.

Table III.1 summarizes the registration errors expected for one band with another. Misregistrations as large as 7.0% of a large detector FOV can be expected.

Simulation Studies

To investigate the effects of misregistration on clear column radiance retrieval numerical simulations of several infrared images were produced. The data grids represent scenes in the Canary Islands and Mexico; they contain an area approximately 400 km^2 and have a resolution of 3.6 km (.1 mrad). Measurements are simulated by weighting the radiances of the grid with the spatial weighting functions representative of the real detector response. The spatial weighting function accounts for the effects of non-zero response time of the detector electronics and diffraction (see Appendix B). Radiances are determined for channel 8 (11.2 micron channel) and channel 5 (13.3 micron sounding channel).

Table III.1 Peak Registration Errors (given in % of large detector FOV)

A.	Different spectral bands using the same detector:	
	1) line start timing	1.4
	2) EA sampling of ET data	1.3
	3) apparent earth motion	3.5*
	4) satellite spin axis notation	1.3
	5) motion of clouds in scene	1.8*
	6) filter cocking	1.1
	7) different	spatial weighting adjusted
B.	Different spectral bands using different detectors	
	0) all of the above	
	1) detector array positioning 2) optical axis not spin axis	5.2
	3) responsivity variations	spatial weighting adjusted
	4) detector size differences	spatial weighting adjusted
	Peak Registration Error	7.0

*assuming 30 sec interval between window and sounding channel observations

Random correlated noise is added to the radiances (noise equivalent radiance is .06 erg/etc for channel 8 and .58 erg/etc for channel 5) and CCRR's are made using the PFOV technique. The results of ten noise additions are averaged and RMS deviations are calculated to give statistical significance to the CCRR errors. Twenty-five percent misalignment in the window band with respect to the sounding band is achieved by shifting the grid over one .1 mrad column and reprocessing the window band radiances. Smaller misalignments are calculated from linear combinations of the 0% and 25% misaligned radiances. Data is analyzed on subgrids of 90×90 km^2, 60×60 km^2, and 30×30 km^2. For each subgrid a gated weighted mean error is processed. The weighted mean is calculated by weighting each pair retrieval radiance by the inverse of its variance. For most subgrids a small number of pairs have CCRR's that are causing a large portion of the mean error. To prevent this, the gated mean is evaluated using only pair retrievals within a standard deviation of the weighted mean. Selection of the best gate was done by maximizing subgrid data acceptability while minimizing the rejection of pair retrievals within each subgrid. For simplicity, the weighted gated mean error will be referred to as the mean error.

Results for the Canary Island Grid (shown in Fig. III.2) are presented in Figures III.3 through III.5. In general, one notices in all of the figures that as the misalignment increases a marked negative bias appears in the mean error. A major part of this bias is a consequence of the PFOV technique and is grid independent. For example, some negative bias occurs when the window channel sees a cloudless FOV and the PFOV technique assumes the misaligned sounding channel FOV is also clear, and then uses a cloudy FOV

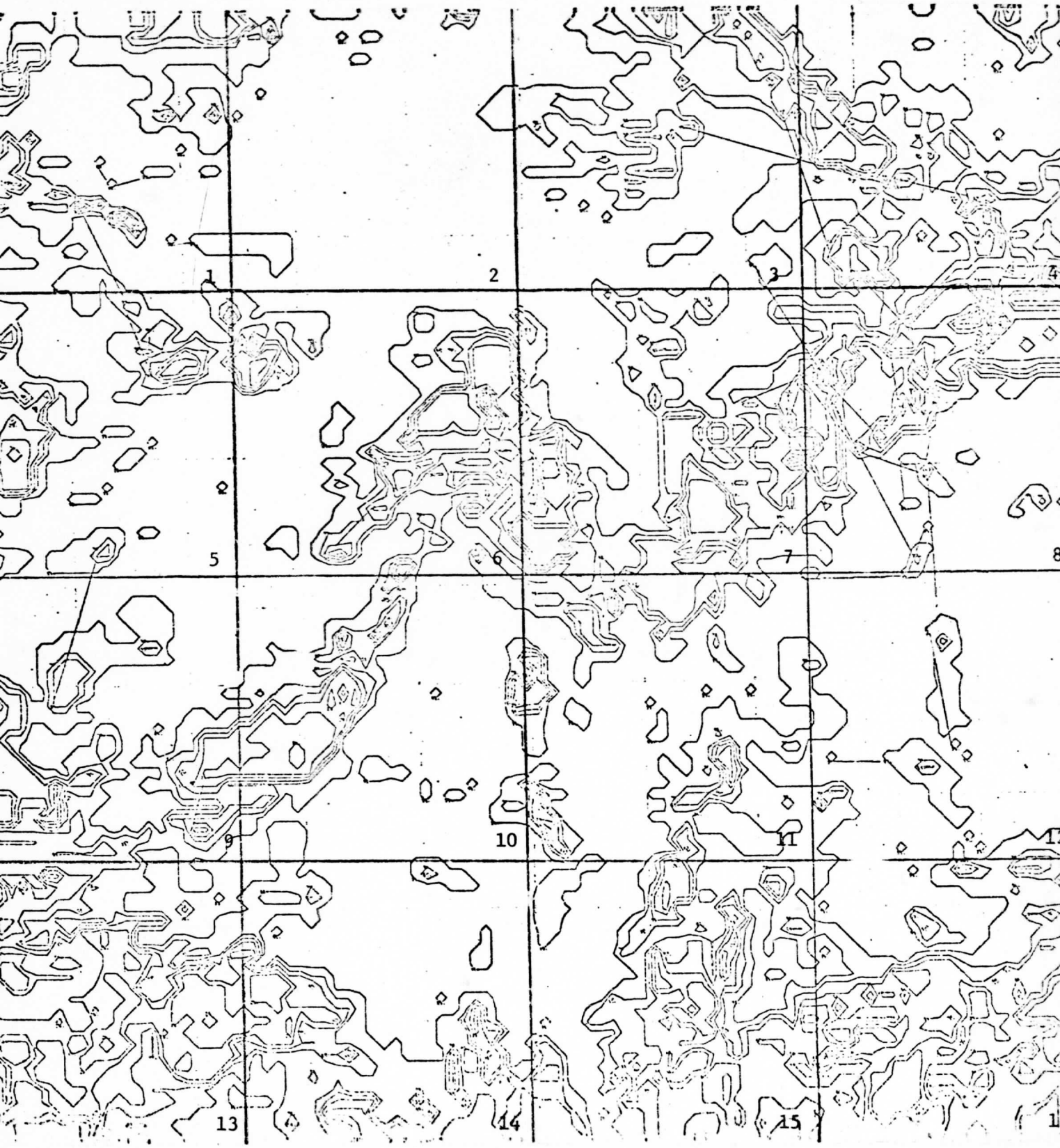

Figure III.2 Depiction of the Canary Island Grid and the sixteen subgrids.

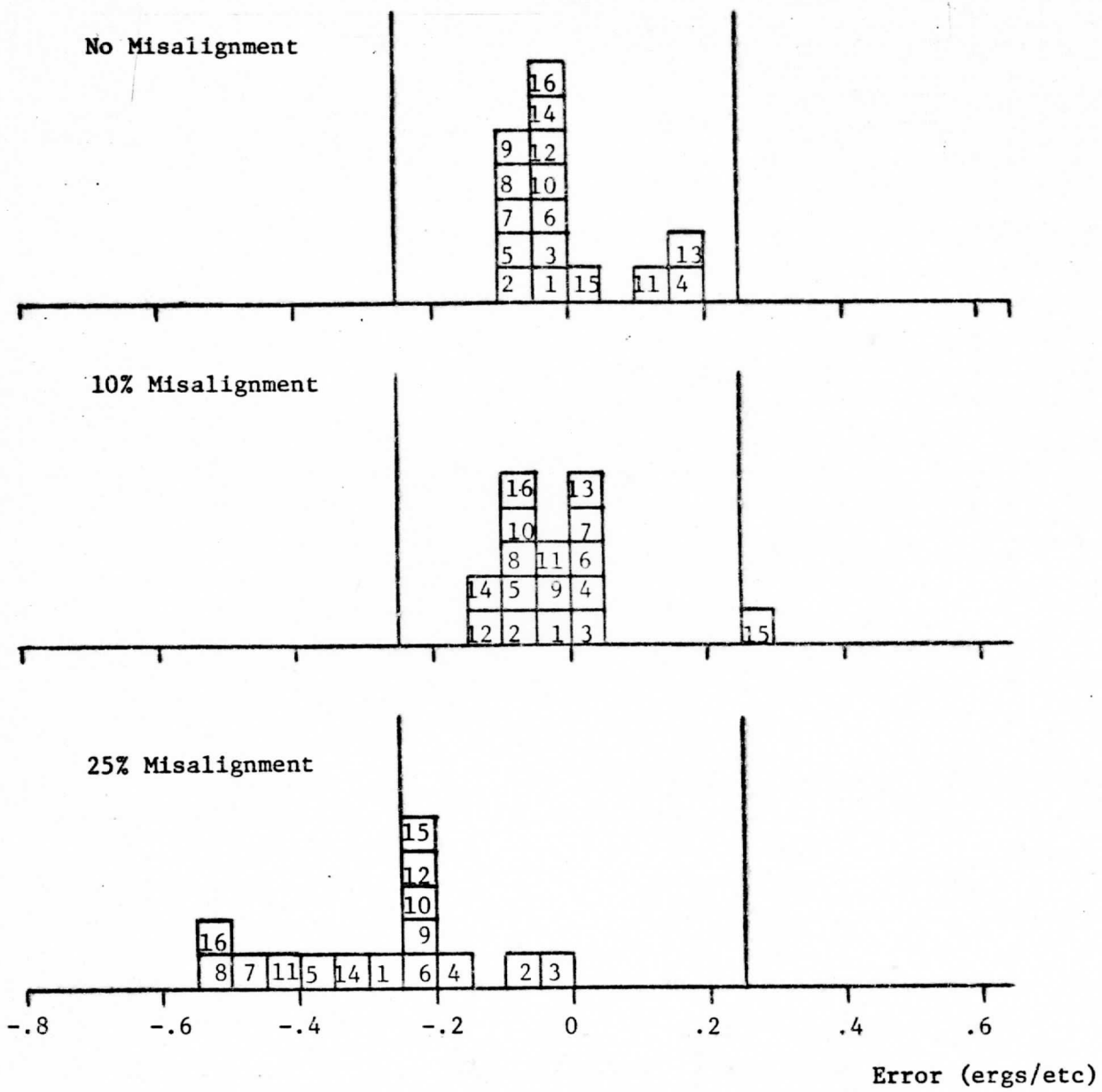

Figure III.3 Mean Error for different misalignments on 90 x 90 km^2 subgrids viewed with the real detector response. The average of ten noise runs is displayed with the average noise RMS per subgrid at .13 erg/etc. The numbers within the histogram are the subgrid numbers.

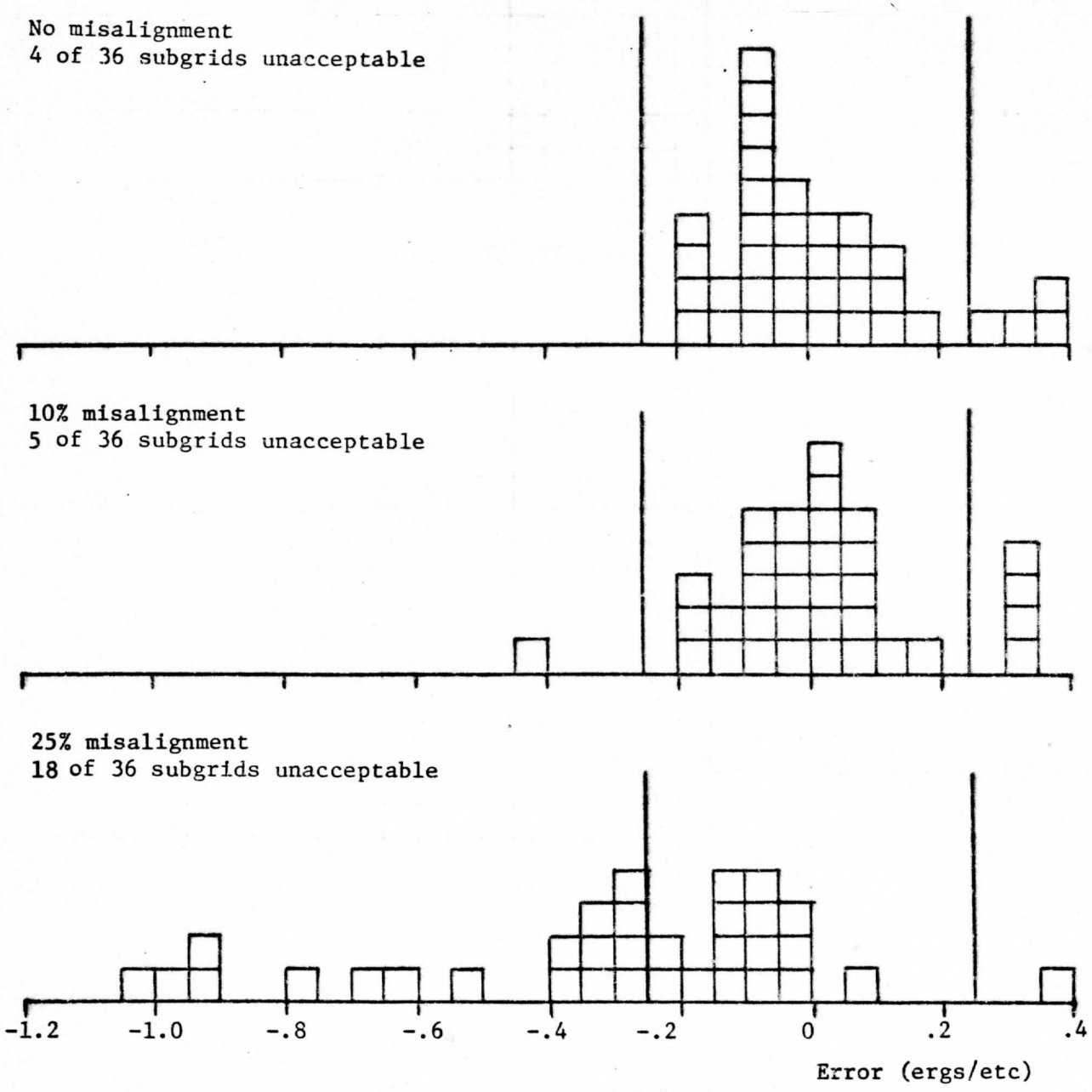

Figure III.4 Mean Error for different misalignments on 60 x 60 km^2 subgrids viewed with the real detector response. The average of ten noise runs is displayed with the average noise RMS per subgrid at .20 erg/etc.

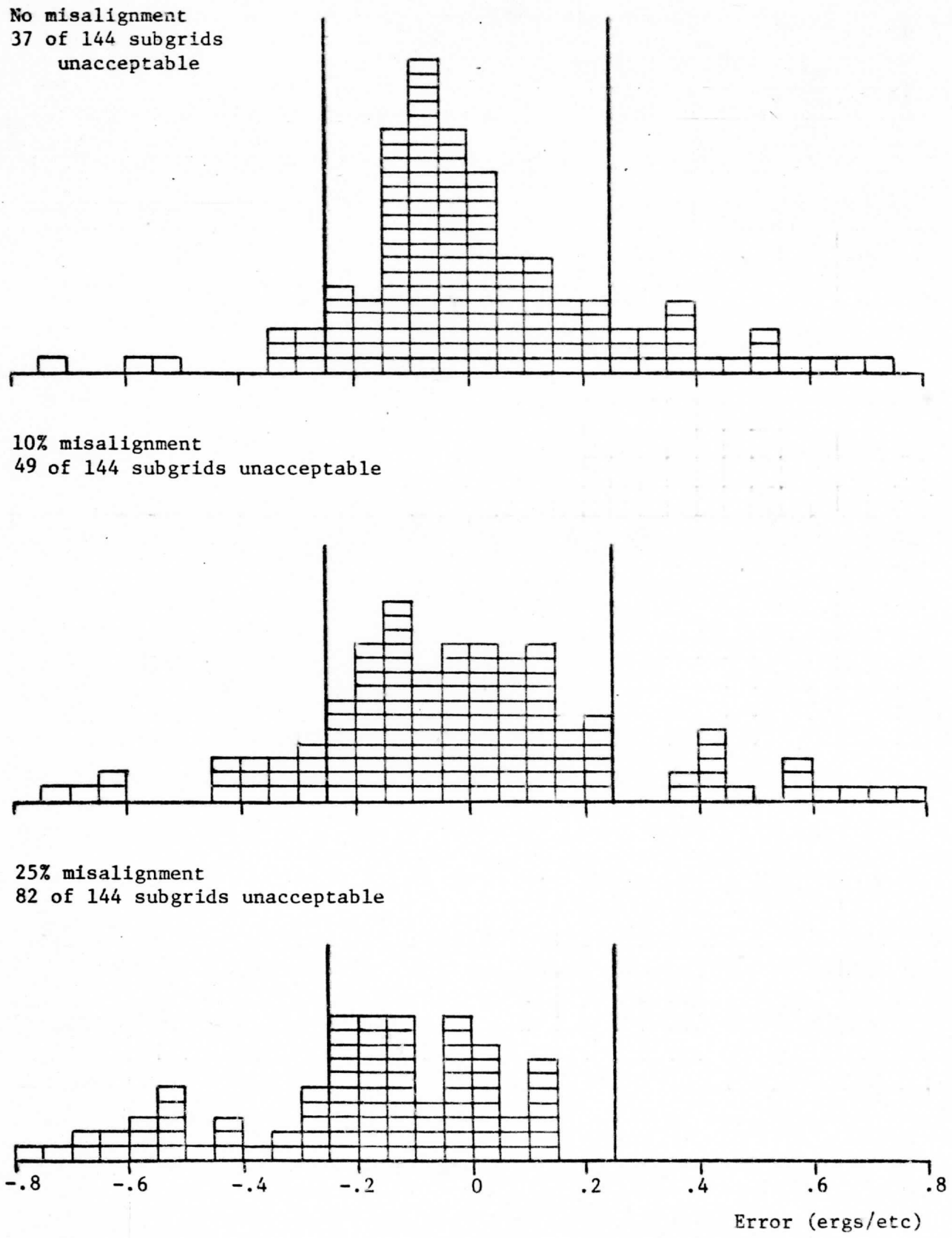

Figure III.5 Mean Error for different misalignments on 30 x 30 km^2 subgrids with real detector response. The average of ten noise runs is displayed with the average noise RMS at .36 erg/etc.

radiance for I^{s}_{cl}. Mean error plots in Figure III.3 for the sixteen 90×90 km^2 demonstrate the following general behavior for small misalignments. When the window channel is misaligned into less cloudy regions, the mean error goes negative as a shift of the cloud line to the right would dictate (e.g., subgrid 13). Shifting the cloud line to the left, clear into cloudy, the mean error should go positive as subgrid 6 demonstrates. At 90×90 km^2 resolution, the mean error of the CCRRs is within the .25 erg/etc requirement that enables useful sounding for up to 10% misalignment, but the results for 25% misalignment are unacceptable. The RMS of the ten noise runs is unaffected by misalignment and stays at .13 erg/etc.

In Figure III.4, similar results for 60×60 km^2 resolution are shown. Roughly eight out of nine subgrids are acceptable at up to 10% misalignment, but only half are acceptable at 25% misalignment. The average noise RMS per subgrid is .20 erg/etc.

Finally at 30×30 km^2 resolution (Fig. III.5), one fourth of the subgrids are unacceptable with no misalignment, one third with 10% misalignment, and two thirds with 25% misalignment. The noise RMS per subgrid is .36 erg/etc, well above the tolerable level.

Conclusions

All of the simulations shown have been performed with the Canary Island Grid. Similar tests have also been done with the Mexico Grid and the results are comparable. The same conclusions can be drawn from either grid and they are:

(1) For the current data acquisition scheme, peak misalignments of 5% to 10% of a large detector FOV can be expected.

(2) The .25 erg/etc requirement on CCRR accuracy is achievable for resolutions as small as 60×60 km^2 and misalignments as large as 10%. Sounding at resolutions of 30×30 km^2 will require reduced noise RMS and selection of relatively cloud free areas.

(3) Detection of cloud types by time sequence window channel scenes may help reduce the occurrence of mixed cloud type pair projections, hence reduce errors. Preliminary investigations show that if the Canary Island grid is assumed to contain only one cloud type, then mean errors in PFOV retrievals are reduced by a factor of four for misalignments of 10% or less.

APPENDIX A. VAS-D GENERAL INFORMATION

Filter Wheel and Detectors

The VAS-D has six detectors that detect infrared radiation in 12 spectral bands. Insertion of a filter wheel in front of the detector package makes this possible. The filter wheel is used in the generation of multispectral or dwell sounding images. Each of its 12 positions corresponds to a different spectral band. Table A.1 indicates the filter wheel spectral bands and the dwell sounding sequence. Two bands sense the atmosphere in the window regions (11.2 micron and 3.9 micron), three bands sense in the H_2O spectral regions, and the remaining seven bands sense in the CO_2 spectral regions. Figure A.1 shows the detector array. Two detectors have a subpoint resolution of 6.9 km (IGFOV of 0.192 mr on a side) and are used primarily for imaging. Four detectors have a resolution of 13.8 km (IGFOV of 0.384 mr) and are used for imaging or sounding information. The two small infrared channel detectors are mercury-cadium-telluride (HgCdTe) long-wavelength detectors. Two of the large infrared channel detectors are HgCdTe. The other two are indium antimonide (InSb). Although there are six VAS infrared detectors, only two will be in use during any satellite spin period. Pairs of channels -- the small HgCdTe channels, the large HgCdTe channels, or the InSb channels -- will be automatically switched by the VAS processor depending on the selected mode of operation.

Dwell Sounding

The dwell sounding mode has 3 submodes. They are submode 1, submode 2, and submode 3. They occur in the cyclic order 1, 2, 3, 2, 1, 2, 3, 2; etc. thoughout the frame. A brief explanation of the submodes follows.

Table A.1 VAS-D Spectral Bands and Sounding Sequence

Band	λ (Microns)	Δ[a]	Dwell Sequence	Detector	Region of Sensitivity
1	14.707	.216	12	HgCdTe	CO_2
2	14.453	.334	11	HgCdTe	CO_2
3	14.227	.324	10	HgCdTe	CO_2
4	13.989	.391	8	HgCdTe	CO_2
5	13.309	.356	7	HgCdTe	CO_2
6	4.516	.092	2	InSb	CO_2
7	12.660	.321	5	HgCdTe	H_2O
8	11.242	1.759	6	HgCdTe	window
9	7.248	.210	9	HgCdTe	H_2O
10	6.728	.677	3	HgCdTe	H_2O
11	4.436	.079	1	InSb	CO_2
12	3.940	.217	4	InSb	window

[a] half amplitude band width

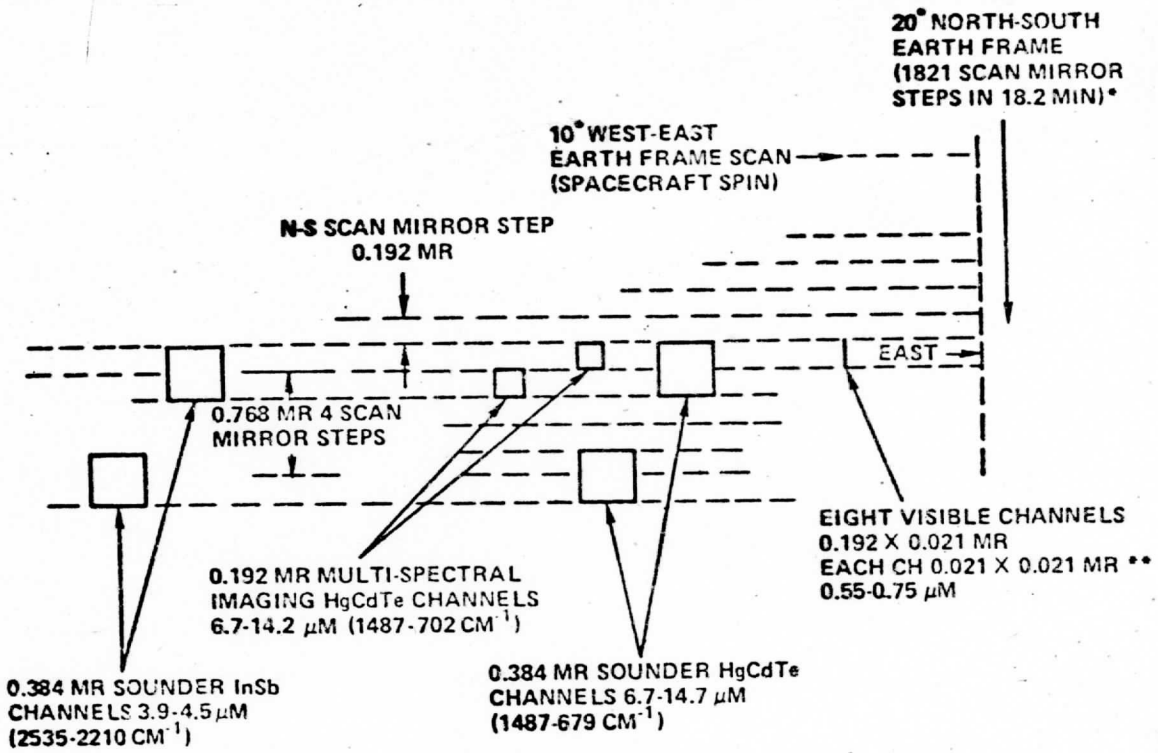

NOTE: ONE INFRARED DETECTOR PAIR USED DURING EACH SCAN LINE

* NORMAL VISSR AND MULTISPECTRAL IMAGING MODE
** 0.021 X 0.021 MR GOES D, 0.020 X 0.025 MR GOES E, F

Figure A.1 VAS-D Detector Package Array

Submode 1 (without visible):

One satellite spin occurs per scan mirror step. After each mirror step, data is transmitted from the two small (6.9 km) band 8 (11 μm) channels. This mode is programmable to have 1 to 8 scan mirror steps.

Submode 1 (with visible):

Two satellite spins occur per scan mirror step. During the first spin (after the step) data is transmitted from the two small (6.9 km) band 8 (11 μm) channels. During the second spin two channels of visible data are transmitted. The first channel of visible data is an average of the 4 north visible detectors (see Figure A.1), and the second channel is an average of the 4 south visible detectors. This mode is programmable to have 1 to 8 scan mirror steps.

Submode 2:

This is the dwell mode. The scan mirror does not step during this mode. During this mode each of the 12 spectral filters may be put into the optical train and held there for from 0 to 255 satellite spins. The number of spins for each spectral band is programmable.

Submode 3:

This is the same as submode 1, except the number of scan mirror steps may be different than submode 1.

If $S_1(S_3)$ is the number of scan mirror steps in submode 1 (3) and S_2 is the number of dwell spins in submode 2, then the time required for each (1,2,3,2) sounding cycle is

$$T_{wo} = (S_1 + 2S_2 + S_3)t \qquad \text{(A.1)}$$

$$T_w = (2S_1 + 2S_2 + 2S_3)t \qquad \text{(A.2)}$$

where wo indicates without visible data, w indicate with, and t is the nominal spin period of the satellite (.01 minutes). The north-south

spatial coverage of each scan mirror step at the subsatellite point is 6.9 km, so the north south extent of a latitude swath covered during one sounding cycle is

$$X_{NS}=(S_1 + S_3)\ 6.9\ \text{km}. \qquad \text{(A.3)}$$

The sounding rate is the ratio;

$$S_{wo}=6.9\ (S_1 + S_3)/(S_1 + 2S_2 + S_3)/t\ \ \text{km/min}, \qquad \text{(A.4)}$$

$$S_w=6.9\ (S_1 + S_3)/(2S_1 + 2S_2 + 2S_3)/t\ \text{km/min}. \qquad \text{(A.5)}$$

Figures A.2 and A.3 illustrate two scan patterns that enable contiguous dwell sounding using the spin budget developed in Section II. The sounding rates for either scan pattern are approximately the same and are 30.3 km/min without visible data, 29.1 km/min with visible data.

Multispectral Imaging

In the multispectral imaging (MSI) mode the scan mirror steps after each satellite spin. In this mode images may be formed using either one set small detectors and two sets of large detectors or four sets of large detectors. The first mode can provide the normal VISSR cloud mapping function. In addition, it can supply data in any two additional spectral bands selected with a spatial reoslution of 13.8 km. This mode of operation takes advantage of the condition that the VAS infrared imaging detectors (small HgCdTe) are offset one scan line in the N-S plane. Using the data from these detectors simultaneously produces a complete infrared map when they are operated every other scan line. This allows using the larger detectors during half of the imaging/scanning sequence period to obtain additional spectral information. Figure A.4 shows the two MSI scan patterns that yield contiguous coverage. Full Disk images of 1821 scan lines require 18.21 minutes for completion.

DWELL SOUNDING SCAN PATTERN
MIRROR STEPPING - FILTER SELECTION SUBROUTINE SET AT
(6-DWELL - 2-DWELL)

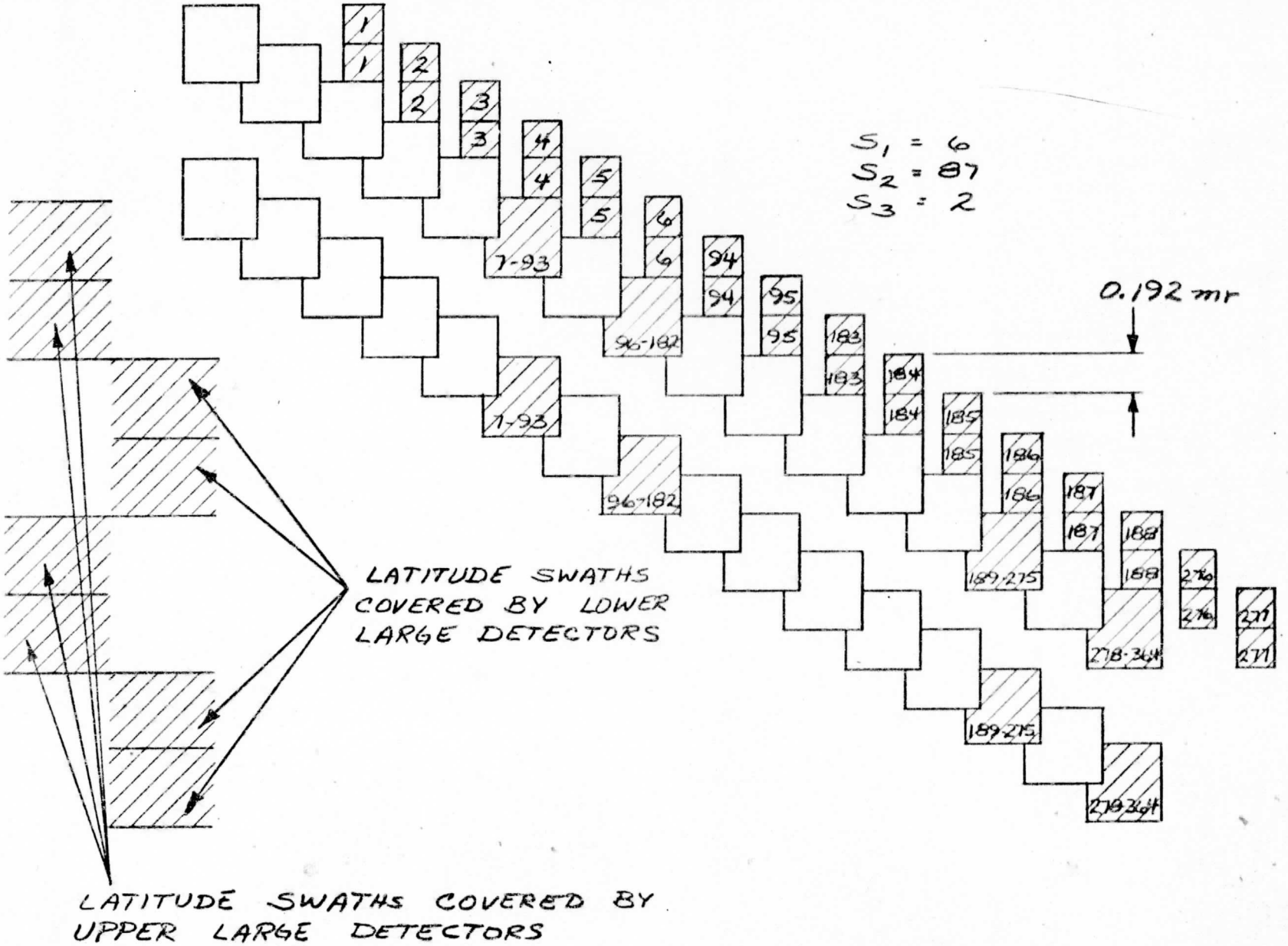

FIGURE A-2 SCAN PATTERN FOR CONFIGURATION 1

DWELL SOUNDING SCAN PATTERN
MIRROR STEPPING - FILTER SELECTION SUBROUTINE SET AT
(2-DWELL - 2-DWELL)

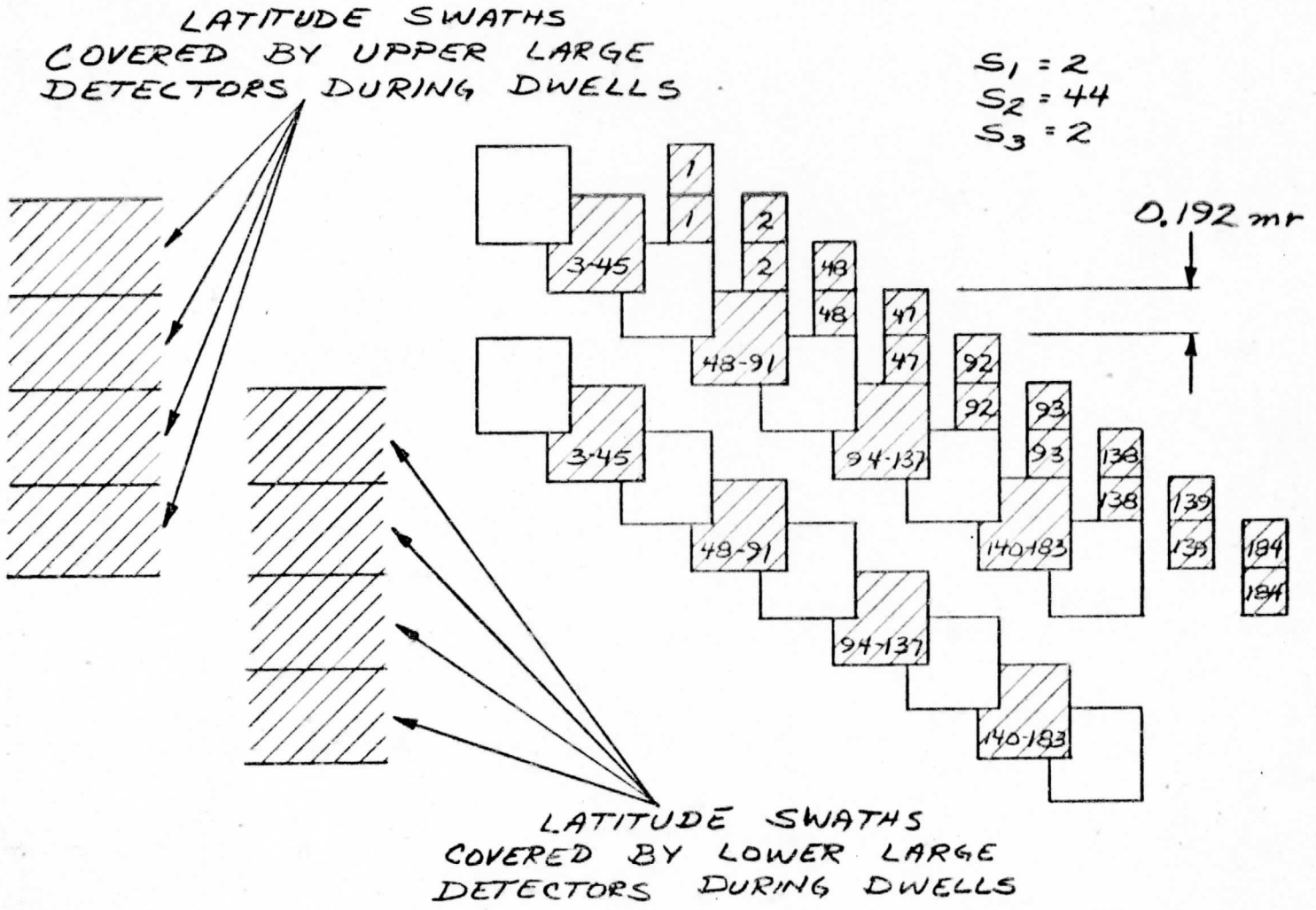

FIGURE A-3 SCAN PATTERN FOR CONFIGURATION 2

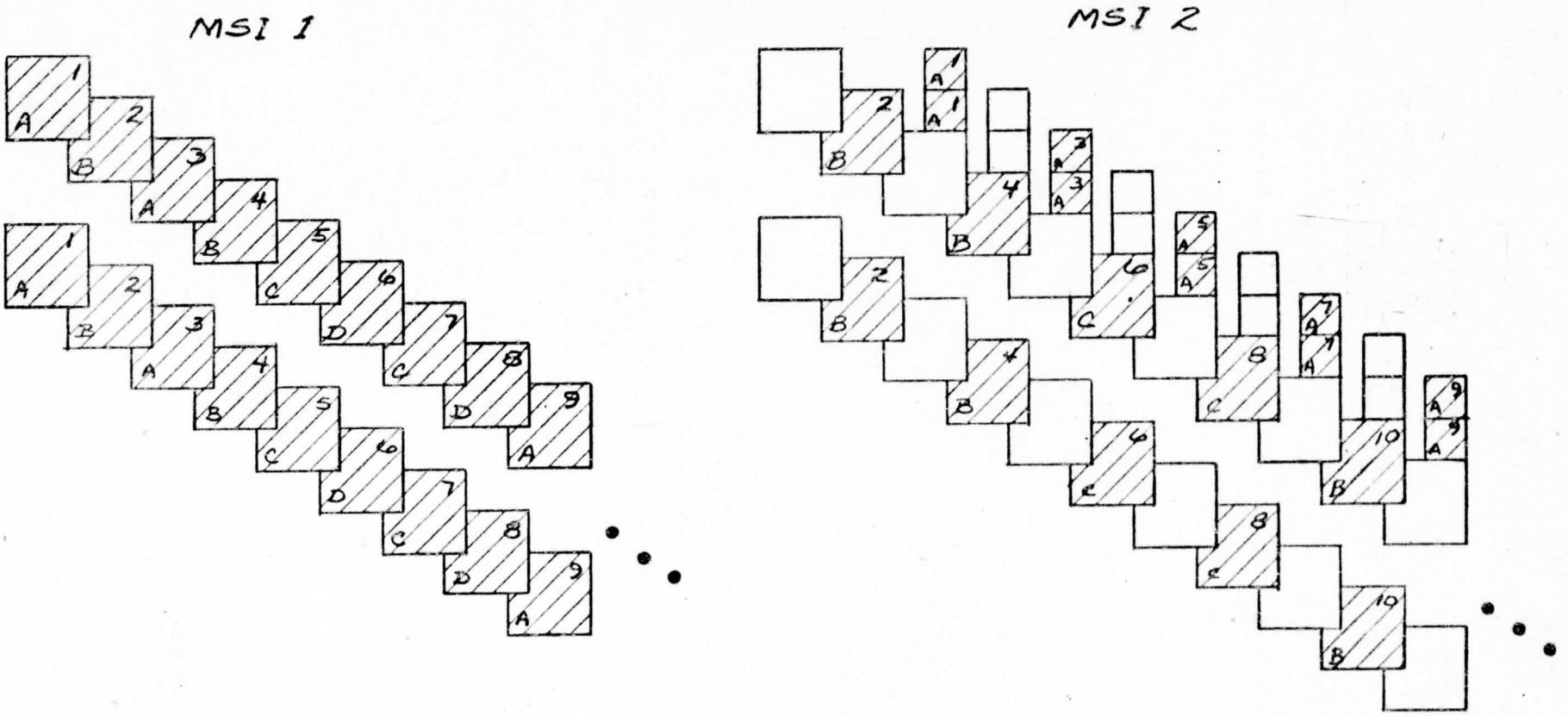

FIGURE A.4 SCAN PATTERNS FOR MULTISPECTRAL IMAGING

On Board Processor

The VAS is operated in the multispectral imaging (MSI) or dwell sounding (DS) modes by commanding a processor on board the spacecraft. The VAS under processor operation is controlled by 39 parameters (184 bits); see Table A.2. Detailed explanation of the processor can be found in the Synchronizer Data Buffer System Design Report prepared by Westinghouse.

Table A.2 Processor Parameters

Parameter	Description	Coding
P1	MSI/D-S Mode	1 MSI 0 D-S
P2	MSI Spectral Band A	0000 Spectral Band 1 0101 Spectral Band 7
P3	B	1011 Spectral Band 2 1000 Spectral Band 8
P4	C	0100 Spectral Band 3 0001 Spectral Band 9
P5	D	0010 Spectral Band 4 0111 Spectral Band 10
P6	E	1010 Spectral Band 5 0011 Spectral Band 11
P7	F	0110 Spectral Band 6 1001 Spectral Band 12
P8	G	
P9	H	
P10	MSI Band No. 8 FOV Size	1 Large 0 Small
P11	D-S Submode 1 Number of Steps	000 1 Step 111 8 Steps
P12	D-S Submode 2 Dwell Spins for Band 1	
P13	2	
P14	3	
P15	4	
P16	5	
P17	6	00000000 Skip Band
P18	7	11111111 255 Spins
P19	8	
P20	9	
P21	10	
P22	11	
P23	12	
P24	D-S Submode 3 Number of steps	000 Step 111 8 Steps
P25	D-S Submode 2 Band 3 FOV	
P26	4	
P27	5	
P28	6	0 Small
P29	7	1 Large
P30	8	
P31	9	
P32	10	
P33	D-S Submode 2 PMT On/Off	0 On 1 Off
P34	Scan Direction South/North	0 South 1 North
P35	Electronics Calibration Off/On	0 Off 1 On
P36	Frame Start Line Number	2048 Plus Scan Line Number
P37	Frame End Line Number	2048 Plus Scan Line Number
P38	D-S Multiplex Mode Off/On	0 Off 1 On
P39	Spare	

APPENDIX B. DETERMINATION OF SPATIAL WEIGHTING CHARACTERISTICS OF THE VAS INSTRUMENT

In the case of an ideal diffraction free step scan radiometer, the detector output is proportional to the direct average of the scene radiance over the geometrical field of view of the detector. In the case of the VAS radiometer, the detector output is filtered so that each measurement is an unequally weighted time average of the field swept out by the detector FOV. In addition, diffraction effects reduce the detector response to scene radiances within the IGFOV and increase its response to scene radiances outside the IGFOV. Both effects can be simultaneously described by a spatial weighting function $\phi(x,y)$ which is defined so that the detector response $I(t)$ at time t is given by

$$I(t) = \int_{-\infty}^{\infty} dx \int_{\infty}^{\infty} dy \; \phi[x - x_o(t),\; y - y_o(t)]I_s(x,y) \qquad (B.1)$$

where x and y are coordinates of the scene and $x_o(t)$ and $y_o(t)$ are the scene coordinates of the spatial weighting peak at time t. This point follows the scanning IGFOV but lags behind because of the prealiasing filter at the detector output. Since the detector response $I(t)$ must equal the scene radiance I_s when the scene is flat, $\phi(x,y)$ must satisfy the normalization condition

$$\int_{-\infty}^{\infty} dx \int_{-\infty}^{\infty} dy \; \phi(x,y) = 1. \qquad (B.2)$$

The net spatial weighting function can be calculated from the impulse response function $R(t)$ and the diffraction weighting function $D(x,y)$ according to the following equation

$$\phi(x,y) = N \int_{-\infty}^{\infty} dx' \; R\left\{\frac{x - x'}{v}\right\} D(x - x', y) \qquad (B.3)$$

where v is the scene velocity of the detector IGFOV, R $(\frac{x-x'}{v})$ is the fraction of the filter output at time x/v due to detector input at time x'/v, D(x-x',y) is the fractional energy emitted by the scene from (x,y) which falls on the detector while its IFOV is centered at (x',y), and N is a normalization factor adjusted so that $\phi(x,y)$ satisfies equation (B.2). It is assumed that the detector IGFOV scans in the positive x' direction.

The impulse response function is calculated from the characteristics of the prealiasing filter. This is assumed to be a five-pole Bessel low pass filter with pole locations

$$P_1 = -3.646739,$$

$$P_{2,3} = -3.351956 \pm i\ 1.742661,$$

$$P_{4,5} = -2.324674 \pm i\ 3.571023,$$

and 3 db cutoff frequency at 26 KHz. The impulse response function is obtained from the equation

$$R(t) = \frac{1}{2\pi} \int_{-\infty}^{\infty} H(i\omega) e^{i\omega t} d\omega \qquad (B.4)$$

where

$$H(p) = 945./[(p-p_1)(p-p_2)(p-p_3)(p-p_4)(p-p_5)]. \qquad (B.5)$$

Results of this complex integration are shown in Fig. B.1. Note that the filter output at time t = 0 is mainly determined by signals input at a time 14 μsec earlier and entirely unrelated to signals input at times $t \geq 0$ (the future does not influence the present).

The diffraction weighting function is calculated from the equation

$$D(x,y) = \int_{A_d} d\xi' d\eta' I_d\{[\xi(x) - \xi']^2 + [\eta(y) - \eta']^2\} \qquad (B.6)$$

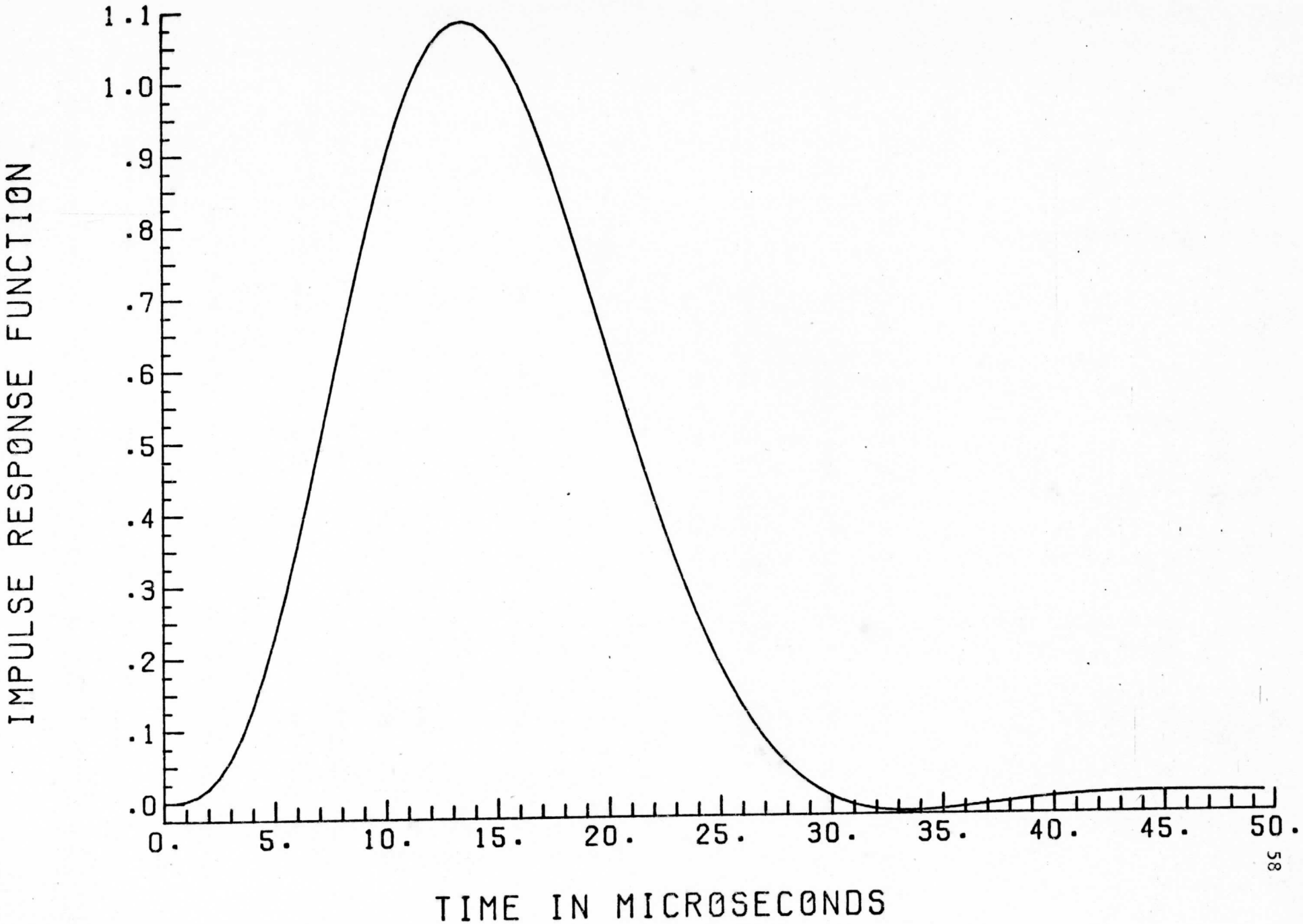

Figure B.1 Impulse response function as a function of time. The positive values refer to time previous to the current IGFOV center.

where the integral is taken over the detector area A_d; $\xi(x)$ and $\eta(y)$ are projections on the focal plane of the scene position (x,y); and $I_d(r)$ is the diffracted intensity on the focal plane at a distance r from the geometrical projection of a point source in the scene. The diffracted intensity is that of an annular aperture and is given by (Born, 1965)

$$I_d(r) = \frac{I_o}{(1-\varepsilon^2)^2} \left[\left(\frac{2J_1(\rho)}{\rho}\right) - \varepsilon^2 \left(\frac{2J_1(\varepsilon\rho)}{\varepsilon\rho}\right)\right]^2 \qquad (B.7)$$

where

$\rho = 2\pi\frac{a}{\lambda} \sin r$

a = outer aperture radius (20.3 cu for VAS scan mirror)

λ = wavelength of diffracted radiation (12 VAS spectral bands)

ε = obscuration ratio (.4 for VAS secondary mirror)

J_1 = the first order bessel function

I_o = the intensity at the center of the pattern (r=o).

A cross section of the resultant diffraction weighting function D(x,y) is plotted in Figure B.2 for four of the twelve VAS spectral bands (3.94, 6.73, 11.24, and 14.71 microns). Note that the detector size differs for InSb (.425 mrad square) and for HgCdTe (.384 mrad square). The cross section displayed in these plots represents the intersection of D(x,y) with a plane passing through the center of the IGFOV (x=0, y=0), perpendicular to the x,y plane and parallel to one of the four detector edges. The horizontal coordinate is measured in milliaradians from the center of the IFGOV.

As this figure shows, not all of the energy emitted by sources near the center of the IGFOV and collected by the sounder optics strikes the detector surface. For the 11.24 micron radiation from sources at the

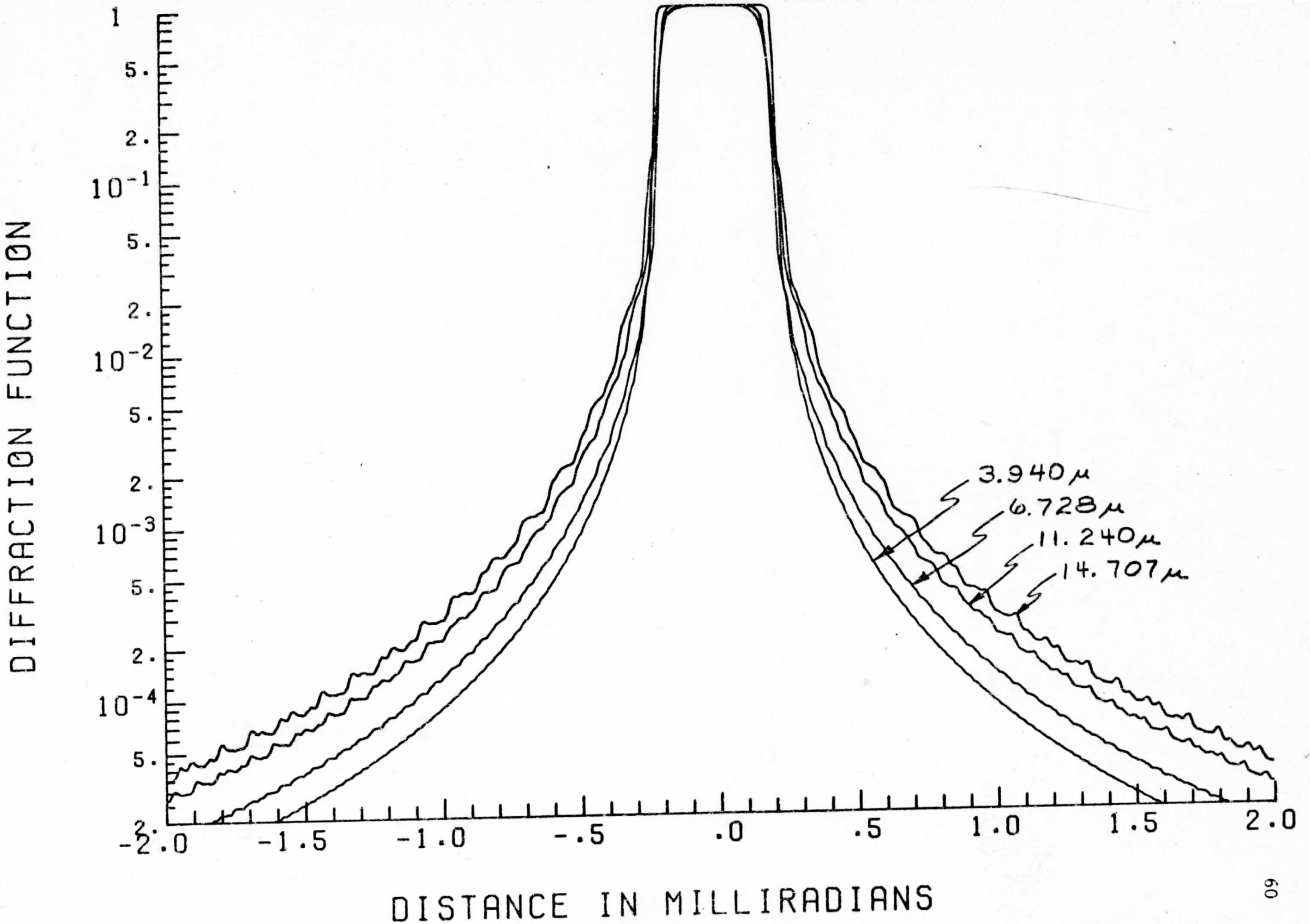

Figure B.2 The diffraction function for four of the VAS spectral bands. The horizontal coordinate is measured in milliradians from the center of the IGFOV.

IGFOV center 95.5% strikes the detector surface; from sources 4 mr from the IGFOV center the fraction is down to .5%. The percentages for the other wavelengths are comparable. The magnitude of the effect of diffraction is summarized in Table B.1 for these same wavelengths. The amount of detector response originating from inside a circle of varying radius is tabulated. For the 11.24 micron radiation a significant portion of the detector response (.1%) comes from outside of a circle of radius 9.32 mr (or 334 km for an IGFOV at the subsatellite point).

Integrating the impulse response function over the diffraction weighting function according to equation (B.3) yields the net spatial weighting function of the VAS sounder, i.e. $\phi(x,y)$, if the detector responsivity is assumed to be uniform. For the VAS large HgCdTe and InSb detectors a 10% drop off in the peak response from east to west is also accounted for. The spatial weighting functions for bands 1, 8, 10, and 12 are shown in Figure B.3.

The plots represent east-west slices of ϕ; since we are assuming a uniform detector responsivity the north-south slices are identical to the diffraction functions. The oscillations noticeable in the semilog plots are caused by oscillations of the impulse response function and are largest for channels where the diffraction function falls off the sharpest. For very large angles, ϕ and D become essentially identical because the impulse response function is a sharply peaked function.

Table B.1 Effective Detector FOV for Several VAS Wavelengths

Fraction of total response originating from within a circle of indicated radius (mr).

λ(microns)	50%	80%	90%	99%	99.9%
for .384 mr HgCdTe detector					
14.707	.146	.195	.240	1.220	12.20
11.242	.143	.188	.221	.932	9.32
6.728	.140	.179	.195	.558	5.58
For .425 mr InSb detector					
3.94	.149	.190	.203	.301	3.01

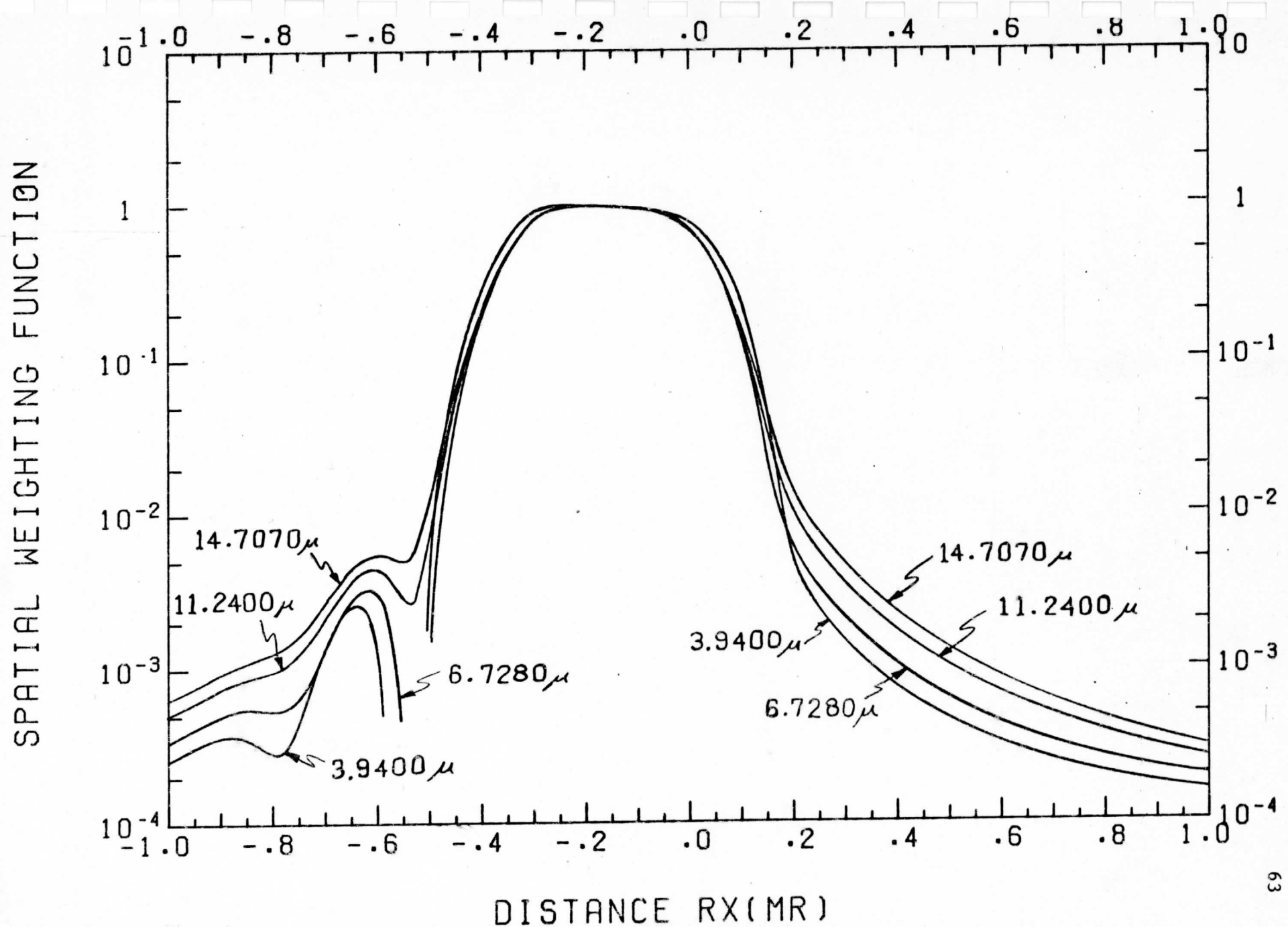

Figure B.3 The spatial weighting function for four of the VAS spectral bands. The horizontal coordinate is measured in milliradians from the center of the IGFOV.

APPENDIX C. ANALYSIS OF COVARIANCE TO DETERMINE REGRESSION COEFFICIENT

Working with the 28 data sets of the Calibration and Acceptance Test, the relative error for the i^{th} gradient is written

$$(N_T^A - N_T^M)_i - \frac{1}{28} \sum_{k=1}^{28} (N_T^A - N_T^M)_k = R_i \tag{C.1}$$

and the j^{th} telescope component gradient radiance deviation from its mean is written

$$(R_{bb} - R(T_j))_i - \frac{1}{28} \sum_{k=1}^{28} (R_{bb} - R(T_j))_k = \Delta_{ij}. \tag{C.2}$$

If the change in the j^{th} coefficient is written d_j then

$$R_i = \sum_j \Delta_{ij} d_j. \tag{C.3}$$

In the regression solution we minimize the sum of the squared residuals by varying d_j; therefore,

$$\frac{\partial}{\partial d_k} \left\{ \sum_i (R_i - \sum_j \Delta_{ij} d_j)^2 \right\} = 0, \tag{C.4}$$

which leads to the familiar regression solution

$$d_k = \sum_{ij} (\Delta^T \Delta)^{-1}_{kj} \Delta^T_{ji} R_i, \tag{C.5}$$

or

$$\vec{d} = (\Delta^T \Delta)^{-1} \Delta^T \vec{R}. \tag{C.6}$$

To determine explicity the relationships between the ten coefficients determinable from the calibration data set rewrite the regression solution for $\vec{d}$ in terms of the eigenvalues, Λ, and eigenvectors, ϑ, of the covariance matrix, $n^{-1}\Delta^T\Delta$, where n is the number of data samples (for the calibration data set n = 28);

$$\vec{d} = n^{-1} \vartheta \Lambda^{-1} \vartheta^T \Delta^T \vec{R}. \tag{C.7}$$

When the square root of the eigenvalue of the covariance matrix is less than the accuracy of the radiance measurements (.2 to .3 erg/etc), its contribution to $\vec{d}$ is not reliable. The following equations are constructed to determine $\vec{d}$;

$$\partial^T \vec{d} = n^{-1} \Lambda^{-1} \partial^T \Delta^T \vec{R}. \tag{C.8}$$

Then if it is assumed that all coefficients are known except C_{BF} and C_{SMS}, one can construct at least two equations for the two unknowns d_{BF} and d_{SMS} if the gradients of the test data are sufficiently uncorrelated.